High–precision determination of carbon stable isotope in silicate glasses by secondary ion mass spectrometry: Evaluation of international standards

Hyunjoo Lee[a,*], Yves Moussallam[a,b], Estelle F. Rose−Koga[c], Laurette Piani[d], Johan Villeneuve[d], Nordine Bouden[d], Andrey A. Gurenko[d], Brian Monteleone[e], Glenn A. Gaetani[e]

[a] *Lamont−Doherty Earth Observatory, Columbia University, New York, USA*

[b] *American Museum of Natural History, Department of Earth and Planetary Sciences, NY 10024, New York, USA*

[c] *ISTO, UMR 7327, Université d'Orléans−CNRS−BRGM, 1A rue de la Férollerie, 45071 Orléans cedex 2, France*

[d] *Centre de Recherches Pétrographiques et Géochimiques (CRPG), UMR 7358, CNRS−UL 15 rue Notre Dame des Pauvres, 54500 Vandœuvre−lès−Nancy, France*

[e] *Dept Geology and Geophysics, Woods Hole Oceanographic Institution, Woods Hole, MA 02543, USA*

Corresponding author: Hyunjoo Lee; hl3507@columbia.edu

The paper is a non-peer reviewed preprint submitted to EarthArXiv. This manuscript has been submitted to *Chemical Geology a*nd is currently under peer review there.

Abstract

Secondary ion mass spectrometry (SIMS) has been used for isotope analysis of volatile components dissolved in silicate melts for decades. However, carbon *in situ* stable isotope analysis in natural silicate glasses has remained particularly challenging, with the few published attempts yielding high uncertainties. In this context, we characterized 31 reference silicate glasses of basaltic and basanitic compositions, which we then used as standards to calibrate $\delta^{13}C$-value analyses in silicate glasses by SIMS. This set of standards covers a wide range of CO_2 concentrations (380 ppm − 12000 ppm) and $\delta^{13}C$ values (−28.1±0.2 to −1.1±0.2 ‰, ±1σ). The standard sets were analyzed using large−geometry SIMS at two ion microprobe facilities to test reproducibility across different instrumental setups. The instrumental mass fractionation (IMF) varied widely with two different large−geometry SIMS instruments as well as with different analytical parameters such as field aperture size and primary beam intensity. We found that a precision better than ±1.1 ‰ (both average internal and external precision, ±1σ) could be achieved using a primary beam intensity of less than 5 nA, resulting in a final spot size of 10–20 µm, allowing precise analysis of $\delta^{13}C$ in mineral−hosted melt inclusions. This level of precision was achieved at CO_2 concentrations as low as 1800 ppm. This advance opens a wide range of new possibilities for the study of $\delta^{13}C$-value in mafic melts and their mantle sources. The reference glasses are now available at the CNRS–CRPG ion microprobe facility in Nancy, France and will be deposited at the Smithsonian National Museum of Natural History, Washington, USA where they will be freely available on loan to any researcher (*catalogue numbers will be available for the final version of this manuscript*).

Keywords: SIMS; Ion probe; Carbon isotopes; $\delta^{13}C$−value; CO_2

Highlights

- Developed 31 reference glasses of basaltic and basanitic compositions covering broad ranges of CO_2 and $\delta^{13}C$
- Precision <1‰ achieved at 10µm beam size
- Instrumental mass fractionation for carbon isotopes was corrected for variations in matrix composition, beam current, drift, and aperture size

1. Introduction

The measurement of the isotopic compositions of volatile species, such as δ^2H, $\delta^{13}C$, $\delta^{34}S$, and $\delta^{37}Cl$, in silicate glass has typically been performed by bulk rock analysis, such as vacuum extraction or elemental analyzer coupled to mass spectrometry (e.g., Sakai et al., 1982 for S; Ihinger et al., 1994 for general review; Barnes and Sharp, 2006 for Cl; Cartigny et al., 2008 for CO_2; Loewen et al., 2019 for H_2O). However, analysis at low volatile concentrations and isotope compositions in silicate glass by bulk extraction requires up to several hundred milligrams of material, which is challenging when sample availability is limited. In addition, bulk analyses of low volatile concentrations risk contamination by several unwanted materials such as seawater altered material (e.g., Cocker et al., 1982), adsorbed volatiles (e.g., Barker and Torkelson, 1975), organic impurities (e.g., Mattey et al., 1984), precipitated carbonate or reduced carbon on the vesicle wall (e.g., Mathez and Delaney, 1981), and CO_2 gas in micro−vesicles (e.g., Pineau and Javoy, 1983).

Secondary ion mass spectrometry (SIMS) is an *in situ* micro−analytical technique combining high spatial resolution with high sensitivity that is particularly well suited for determining the concentrations and isotopic compositions of light elements (H, Li, B, C, N, O, S) while overcoming many of the challenges involved with bulk analyses. Despite extensive efforts to analyze the isotopic compositions of volatiles in volcanic glasses such as hydrogen (e.g., Hauri et al., 2002, 2006), sulfur (e.g., Shimizu et al., 2019), and chlorine (e.g., Layne et al., 2004) by the latest generation of SIMS, carbon isotopes have been largely ignored following earlier attempts (Hauri et al., 2002) due to its high background signal (e.g., Ihinger et al., 1994). In addition, the matrix effect for carbon isotope that affects the accuracy of SIMS measurements (e.g., Hauri et al., 2002) remains largely unexplored.

This paper presents new standard sets for calibrating the measurement of isotopic composition and concentration of carbon in mafic silicate glasses over a wide range of carbon isotope ratios and concentrations. We detail the methods used to achieve improved internal precision and reproducibility (down to ± 0.3 ‰, 1σ), allowing analysis of carbon isotopes at the 10 μm scale. We evaluate the validity of the technique and standards, investigate compositional matrix effects, and perform test−measurements of carbon isotope on samples of known composition.

2. Methods

High pressure experiments were conducted using a piston cylinder. Carbon isotopic composition of the fused glasses was determined by an elemental analyzer coupled to isotope ratio mass spectrometry (EA−IRMS), while H_2O and CO_2 concentrations were quantified by Fourier Transform Infrared Spectroscopy (FTIR) at Lamont−Doherty Earth Observatory (USA). The major element compositions were measured by electron microprobe at the American Museum of Natural History (USA).

2.1. Samples

Three different subsets of synthetic silicate glasses were created: 1) mid−ocean ridge basalt (MORB), 2) Basanite, and 3) NBO (see below for explanation). A natural mid−ocean ridge basalt was used as starting material for the MORB series. We selected a sample EDUL_DR75_1_04 (CNRS 000 000 2592) presenting a pillow basalt dredged from the South West Indian Ridge (SWIR) collected at 2650–2900 mbsl (meters below sea level) at 37°51′48″S, 49°20′12″E (https://lithotheque.ipgp.fr/edul.html). The initial composition is 50.1 wt% SiO_2, 1.42 wt% TiO_2, 16.4 wt% Al_2O_3, 10.5 wt% FeO_t, 0.2 wt% MnO, 7.0 wt% MgO, 11.4 wt% CaO, 2.4 wt% Na_2O, 0.2 wt% K_2O, and 0.1 wt% P_2O_5 (Moussallam et al., 2023).

As a starting material for the Basanite series, we used a natural basanite from El Hierro. The sample is a seawater quenched lava balloon, erupted at 100–300 m water depth, and collected at Lat: 27.697°, Lon: 17.993° in 2011–2012 (Longpré et al., 2017). The initial composition is 44.4 wt% SiO_2, 5.0 wt% TiO_2, 13.7 wt% Al_2O_3, 12.5 wt% FeO_t, 0.2 wt% MnO, 8.1 wt% MgO, 10.7 wt% CaO, 3.5 wt% Na_2O, 1.4 wt% K_2O, and 0.5 wt% P_2O_5 (Moussallam et al., 2019).

The NBO series glasses range in compositions from andesite to basalt, having been produced by high−pressure experiments by Lee et al. (2024). A mixture of the El Hierro basanite (Longpré et al., 2017) with varying amounts of SiO_2 and Al_2O_3 powders was used as the starting material.

Test glasses to be validated for IMF correction include natural MORB (DR52; Maevaray, 2017) and additional synthetic glasses (ETNA−glass, Hawaii−glass; Lee et al., 2024). DR52 is a basalt collected from SWIR at a depth of 3550 m at 33.79°E, 56.13°S. ETNA−glass and Hawaii−glass used basalt from Mt. Etna and the Hawaiian volcano, respectively, as starting materials. ETNA−glass and Hawaii−glass are formed in the same way as the NBO series, and detailed

starting materials, experimental, and analytical methods for the NBO series, ETNA−glass, and Hawaii−glass can be found in Lee et al. (2024).

2.2. Experimental methods

To ensure homogeneity and remove pre−existing volatile components from the starting material, the starting powders for each series of glasses were placed in a platinum crucible, melted in the furnace at 1 atmosphere (0.1 MPa) and 1350 °C for 2 hours and quenched. The loss of iron during the melting was found to be insignificant, as the iron composition between the starting material (see 2.1) and the material after the experiment (Table 1) fell within the error range of the electron microprobe (1σ RSD 5%). The resulting glass was then crushed and subjected to another melting cycle under identical conditions for an additional 2 hours. The fused glasses were analyzed by FTIR to confirm the absence of volatiles (see 2.3.2).

Gold−palladium (Au_{80}−Pd_{20}) tubes (40 mm i.d. / 45 mm o.d. / 10 mm long) were used for the high−pressure experiments. Cut and annealed tubes were first triple−crimped, welded shut, and flattened at one end. They were then ultrasonically cleaned in dichloromethane for 30 minutes to remove any organic carbon present on the capsule surface (Mattey, 1991) and stored at 110 °C for at least 24 hours prior to use. A total of 120 mg of starting material, including H_2O and mixed carbon source, was loaded into pre−cleaned capsules. Dihydrated oxalic acid ($C_2H_2O_4{\cdot}2H_2O$; $\delta^{13}C$ = −26.7 ‰ ± 0.2) and dolomite ($\delta^{13}C$ = 2.9 ‰ ± 0.2 ‰) were used as carbon sources. It is assumed that CO_2 adsorption on the carbon source or starting material was insignificant. The two carbon sources were mixed in different ratios to obtain the desired $\delta^{13}C$−value and CO_2 concentration, which were weighed on a microbalance (± 0.001 mg). 1 wt% H_2O was added to ensure that the melt reached the liquidus (Médard and Grove, 2008). The other end of the filled capsules was then closed by triple crimping, welding, and flattening. The flattened final capsule was approximately 6 mm in length (Fig. S1).

All experiments were conducted using a piston−cylinder apparatus at the Lamont−Doherty Earth Observatory (Columbia University) in New York, USA. Run conditions were set in such a way that the melt would be undersaturated with respect to volatiles and above the liquidus (1.5 GPa /1270 °C and 1.0 GPa/1240 °C for the MORB series and 1.5 GPa/1280 °C and 1.0 GPa/1265 °C for the Basanite series). After reaching the target P−T, the experiments were left for 2 hours without any attempt to control the oxygen fugacity. It was then quenched by turning off

149 the electrical power. It took about 5 s to cool to less than 400 °C. The pressure decreased during
150 the quenching, however, the resulting glass was observed to be vesicle-free under the microscope.
151 The filled Au_{80}−Pd_{20} capsule was centered in a 35 mm long cylindrical graphite furnace
152 surrounded by a 6mm length high−density Al_2O_3 sleeve. MgO was used as a spacer to fill the other
153 parts of the graphite furnace. The pressure medium outside of the graphite furnace was 35 mm
154 long cylindrical Pb−wrapped CaF_2. A D−type ($W_{97}Re_3$–$W_{75}Re_{25}$) thermocouple located ~1 mm
155 from the capsule, separated by a 1 mm thick Al_2O_3 wafer, provided accurate temperature readings
156 during the run. The assembly diagram is shown in Figure S1.
157

158 **2.3. Characterization**

159 **2.3.1. $\delta^{13}C$−value analysis by EA−IRMS**

160 The $\delta^{13}C$ values of the synthetic glasses were determined using a Costech elemental analyzer
161 (ECS4010) coupled to a ConFlo IV and Thermo Scientific Delta V plus Isotope Ratio Mass
162 Spectrometer (EA−IRMS) at the Lamont−Doherty Earth Observatory, Columbia University, New
163 York, USA. Prior to analysis, the glasses were carefully picked by hand under a stereomicroscope
164 and then ultrasonically cleaned with dichloromethane for 30 minutes to ensure the removal of any
165 organic contaminants. After cleaning, the samples were dried at 110 °C for a minimum of 24 hours.
166 Accurate amounts of each glass were weighed on a microbalance (± 0.001 mg), encapsulated in
167 3.2 × 4 mm tin capsules, and stored in a desiccator until analysis.
168 The encapsulated samples were combusted at ~1700 °C, over a chromium (III) oxide catalyst
169 in the presence of excess oxygen (25 ml/min). Helium was used as a carrier gas at a rate of 100
170 ml/min. A silvered cobalt/cobalt oxide, placed in the quartz combustion tube, ensured the complete
171 conversion of sample carbon to CO_2 and the removal of residual halogens or sulfur. The CO_2 peaks
172 for each sample were then separated on a gas chromatography (GC) column (operating at 55 °C)
173 prior to analysis by IRMS.
174 The $\delta^{13}C$−values obtained for each sample were calibrated using a three−point regression
175 method against the standards USGS24 (graphite; $\delta^{13}C$ = −16.05±0.07‰, VPDB; United States
176 Geological Survey Reston Stable Isotope Laboratory, 2019a), USGS40 (L-glutamic acid; $\delta^{13}C$ =
177 −26.39±0.04 ‰, VPDB, United States Geological Survey Reston Stable Isotope Laboratory,
178 2019b), and USGS41 (L-glutamic acid; $\delta^{13}C$ = 37.63±0.05‰, VPDB; United States Geological

Survey Reston Stable Isotope Laboratory, 2011), with an average analytical internal error of 0.2 ‰. Craig correction is applied to account for the oxygen isotope effect (Craig, 1957). To ensure instrument performance and monitor drift, one set of standards was analyzed for every ~10 samples.

2.3.2. H_2O and CO_2 concentration analysis by FTIR

H_2O and CO_2 concentrations in the synthetic glasses were determined using a Thermo Nicolet iN10 Fourier Transform Infrared (FTIR) spectrometer at Lamont−Doherty Earth Observatory. The instrument was purged with dry, CO_2−scrubbed air, and measurements were facilitated by a liquid nitrogen−cooled MCT−A detector. Preparation of the glass chips involved double polishing with alumina−coated paper. Chip thicknesses ranged from 15 to 100 μm. Prior to measurement, the chips were washed with acetone to remove residual crystal bond. Thickness was determined by the reflectance method (± 3 μm; Nichols and Wysoczanski, 2007).

Spectra were acquired in the range of 400−8000 cm^{-1} with 256 scans and a resolution of 1 cm^{-1} in transmitted mode. The aperture size was set to 100 μm for both width and height. Each sample was analyzed on 2 to 10 spots to ensure homogeneity of H_2O and CO_2 content. Total water content was determined from the intensity of the OH^- stretching band at approximately 3550 cm^{-1}, while CO_2 concentration was derived from the doublet peak at 1515 cm^{-1} and 1435 cm^{-1}. Peak heights were determined by subtracting from the target spectra the volatile−free glass whose composition matches the target spectra. The absorption coefficients for CO_2 and H_2O were selected from Shishkina et al. (2014) based on their closest match to the composition of the target glass. The effects of H_2O and CO_2 have been taken into account when calculating glass density (Bourgue and Richet, 2001; Lesher and Spera, 2015).

2.3.3. Major element composition analysis by electron microprobe

The major element compositions of the glasses were determined using a Cameca SX5−Tactis electron microprobe at the American Museum of Natural History. An acceleration voltage of 15 kV and a defocused beam of 10 μm were used. Beam currents varied depending on the element, ranging from 4 nA for Na (with a 10 s count time) to 10 nA for others (with 20 s count times). Na analysis was done first to minimize potential Na migration. The instrument was calibrated using natural and synthetic mineral standards and glasses, including potassium feldspar (Al, Si, and K),

rutile (Ti), fayalite (Fe), rhodonite (Mn), olivine (Mg), anorthite (Ca), jadeite (Na), and apatite (P). Major element compositions were obtained by averaging 10 random spots on the glass, and errors were estimated from the standard deviation of the 10 replicate analyses.

2.4. Ion microprobe methods

2.4.1. Sample preparation for SIMS

The background levels in the ion microprobe sample chamber for CO_2 and $\delta^{13}C$−value measurements determine the vacuum quality. To reduce the background interference from carbon, the standards were pressed into indium metal (>99.9% purity). The samples were prepared with crystal bond and single−side hand polished down to 0.3 μm using corundum mats and alumina grit. The crystal bond was then removed with acetone and soaked for several hours. The samples were then embedded in indium metal and pressed overnight to achieve a flat surface. Two twin indium mounts were prepared with pieces of the same glass standard shards for the analysis sessions at Nancy and WHOI, respectively (Fig. S2). The final sample mount surface was cleaned with deionized and Millipore filtered water, dried, and then coated with a ~20 nm gold layer to ensure surface conductivity.

2.4.2. Secondary Ion Mass Spectrometry at CRPG–CNRS–Nancy (2023 December)

Analyses were performed on a CAMECA IMS 1270 ion microprobe at CRPG−CNRS−Nancy, France in December 2023. Before analysis, the mount is left in the airlock of the SIMS for 24 hours prior to the analytical session to reach vacuum conditions $<6\times10^{-9}$ Torr. A Cs^+ primary beam was accelerated using a potential of 10 kV. To maintain optimal signal levels for all standard glasses, the primary intensity was adjusted in the range of 0.2 to 3.6 nA for the detector to receive a signal of ^{12}C within the range of 200,000 to 300,000 counts per second (cps). Average ion yields throughout the session were 68 cps/ppm/nA for ^{12}C and 0.7 cps/ppm/nA for ^{13}C.

Secondary negative ^{12}C and ^{13}C ions were detected with an axial electron multiplier (EM) using a magnetic peak switching technique in mono−collection mode, since the axial EM is more resistant to aging than off−axis EMs. Also, the mono−collection setup was chosen because the main source of analytical error comes from the limited count rate on ^{13}C. ^{18}O was measured on a

Faraday Cup (FC) with 10^{11} Ohm resistor at trolley position H2. The ^{12}C signal was tried to maintain < 300,000 cps to mitigate aging of the EM. Background measurements for the EM and FC were performed at mass 11.8 (trolley position L1) and mass 17.8 (trolley position H1), respectively. The mass resolving power (MRP) was set to 5000, which is sufficient for resolving ^{13}C from $^{12}C^{1}H$, but not so high to unnecessarily cut out the ^{13}C signal. Analysis parameters included a field aperture size of 2500 μm, entrance slit of 100 μm, exit slit of 243 μm, contrast aperture of 400 μm, and L4 aperture of 750 μm. The energy slit was centered and opened to 30 eV.

A 120 second pre−sputtering was performed using a 15 × 15 μm^2 square raster to reduce surface contamination, minimize background counts, and remove the gold layer, followed by analyses on a 10 × 10 μm^2 rastered spot positioned at the center of the gridded clean area. Automatic centering of the transfer deflectors and mass was implemented in the analysis routine. Counting times were set to 4 seconds for EM background, 4 seconds for ^{12}C, 20 seconds for ^{13}C, 4 seconds for FC background, and 2 seconds for ^{18}O. Waiting times between mass measurements were set to 3, 1, 1, 1, and 1 second, respectively. A 89 nanoseconds deadtime for the EM has been determined at the beginning of the analytical session. Each measurement consisted of 30 cycles, resulting in an average analysis time of approximately 30 minutes. Further discussion of precision, accuracy, and drift can be found in the results section.

2.4.3. Secondary Ion Mass Spectrometry at Woods Hole Oceanographic Institution (2024 March)

Analyses were performed on a CAMECA IMS 1280 ion microprobe at the Northeast National Ion Microprobe Facility at the Woods Hole Oceanographic Institution (WHOI). Before measurements, the mount was outgassed for about an hour in an airlock until the pressure reached below 5×10^{-8} Torr. Further outgassing occurred upon insertion into the sample chamber, and analyses began only after the sample chamber pressure reached below 5×10^{-9} Torr. The $^{133}Cs^{+}$ primary beam was accelerated at a potential of 10 kV. The beam current was adjusted within a range of 0.6 to 4.6 nA, depending on the expected CO_2 concentration in each glass, to obtain 300,000 cps of ^{12}C and 3,000 cps of ^{13}C. This adjustment was made to achieve count rates on ^{12}C and ^{13}C that enabled $^{13}C/^{12}C$ measurement precision at or below 1.0 ‰ relative standard error for most glasses.

Secondary ions were counted in multi−collector mode, with different secondary magnet settings and detectors for measuring secondary ions of carbon masses and oxygen reference mass, respectively, within each measurement cycle. ^{12}C and ^{13}C were counted simultaneously using EMs at trolley positions L2 for ^{12}C (deadtime = 63.1 nS) and H2 for ^{13}C (deadtime = 63.7 nS) with the secondary magnet set for axial mass 12.5. A high voltage adjustment was made on the electron multiplier at L2 before each measurement to mitigate the effects of detector aging due to the high ^{12}C signal. ^{18}O was measured on a Faraday Detector with 10^{11} Ohm resistor at trolley position H2, with the magnet set for axial mass 17.9. A 250 μm−wide slit was placed in front of each detector to achieve a mass resolving power of ~5000. Analyses consisted of 30 cycles with count times of 2 seconds for ^{18}O and 20 seconds for ^{12}C and ^{13}C.

For the first three sessions, the focused primary bean was rastered over an area of 15 × 15 μm^2 and pre−sputtered for 120 seconds, then the raster was reduced to 10 × 10 μm^2 during the measurement. Analysis crater diameter ranged from ~15 to just over 20 μm, depending on the primary beam current used. The field aperture of 3000 μm, contrast aperture of 400 μm diameter, and an entrance slit of 200 μm width were applied to the secondary ions. Measurement of presumed very low CO_2 crystals (considered as a background level) yielded ^{12}C and ^{13}C signals that were < 10% of the total ^{12}C and ^{13}C signals measured on most of the glasses, but > 10% in lower CO_2 concentration glasses. Average ion yields for the first three sessions were 65 cps/ppm/nA for ^{12}C and 0.7 cps/ppm/nA for ^{13}C, which is comparable to the session in Nancy.

For the last two sessions days, the analytical procedure was modified to minimize the incorporation of surface and background carbon into the measurements. Although the same primary beam currents were used, the pre−sputter time was increased to 300 seconds and the raster during the pre−sputter was increased to 20 × 20 μm^2. The secondary field aperture size was decreased to 1500 μm in order to block the transmission of surface ions from the center of the sputtering crater. With the increased pre−sputter time and decreased field aperture size, the carbon background contribution, as measured on presumed carbon−free crystals on the mount, was <1 % of the total signal measured on most glasses in the session. Average ion yields decreased for the last two sessions, 36 cps/ppm/nA for ^{12}C and 0.4 cps/ppm/nA for ^{13}C. The total analysis time per spot was approximately 15 minutes. Five spots were measured on each glass shard. Any precision, accuracy, and drift will be further discussed in the results section.

3. Results

3.1. Standard characterization

3.1.1. Major element composition

All major element compositions and standard deviations on 10 repeat analyses are provided in Table 1 and Fig. 1 for all the standard series and test glasses. In all cases the glass composition was found to be homogeneous with a relative standard deviation (RSD) of less than 5 % on most element abundance.

Table 1

Major element (in wt.%) and volatile (CO_2 in ppm and H_2O in wt.%) composition of standard and test glasses. Standard deviation (1σ) of each measurement is provided in parentheses.

Name	Type	CO_2	$\delta^{13}C$	H_2O	SiO_2	TiO_2	Al_2O_3	FeO	MnO	MgO	CaO	Na_2O	K_2O	P_2O_5	Total
CI_Ref_4	MORB[1]	9200	−26.4	1.2	48.3	1.4	17.4	10.5	0.2	7.3	11.3	2.6	0.1	0.2	99.3
		(400)	(0.2)	(0.1)	(0.4)	(0.1)	(1.1)	(0.5)	(0.0)	(0.1)	(0.3)	(0.1)	(0.0)	(0.0)	(0.3)
CI_Ref_6	MORB[1]	5100	−26.2	1.1	49.7	1.4	16.0	10.7	0.2	7.1	11.6	2.6	0.2	0.1	99.7
		(100)	(0.2)	(0.1)	(0.3)	(0.1)	(0.1)	(0.1)	(0.0)	(0.1)	(0.1)	(0.1)	(0.0)	(0.0)	(0.4)
CI_Ref_9	MORB[1]	8000	−6.9	1.6	49.0	1.4	15.8	10.6	0.2	7.2	11.6	2.6	0.2	0.1	98.7
		(300)	(0.3)	(0.1)	(0.2)	(0.1)	(0.1)	(0.1)	(0.0)	(0.1)	(0.1)	(0.1)	(0.0)	(0.0)	(0.4)
CI_Ref_10	MORB[1]	5800	−13.8	0.8	48.6	1.4	15.8	10.8	0.2	7.1	12.4	2.6	0.2	0.1	99.1
		(900)	(0.6)	(0.1)	(0.5)	(0.1)	(0.1)	(0.2)	(0.0)	(0.1)	(0.4)	(0.2)	(0.0)	(0.0)	(0.6)
CI_Ref_11	MORB[1]	7000	−27.4	1.1	49.2	1.4	15.8	11.0	0.2	7.0	11.4	2.5	0.2	0.1	98.8
		(500)	(0.2)	(0.1)	(0.1)	(0.1)	(0.1)	(0.1)	(0.0)	(0.1)	(0.1)	(0.2)	(0.0)	(0.0)	(0.2)
CI_Ref_15	MORB[1]	2300	−7.9	1.0	49.4	1.4	15.9	10.9	0.2	7.2	11.6	2.6	0.2	0.1	99.5
		(300)	(0.2)	(0.1)	(0.2)	(0.1)	(0.1)	(0.2)	(0.0)	(0.1)	(0.1)	(0.2)	(0.0)	(0.0)	(0.3)
CI_Ref_18	MORB[1]	2700	−24.3	1.1	49.5	1.4	16.0	11.1	0.2	7.1	11.5	2.6	0.2	0.1	99.6
		(300)	(0.2)	(0.1)	(0.2)	(0.1)	(0.1)	(0.1)	(0.0)	(0.1)	(0.1)	(0.1)	(0.0)	(0.0)	(0.3)
CI_Ref_20	MORB[1]	2800	−23.1	0.8	49.8	1.3	16.0	11.1	0.2	7.1	11.5	2.5	0.2	0.1	99.9
		(300)	(0.2)	(0.1)	(0.2)	(0.1)	(0.1)	(0.2)	(0.0)	(0.1)	(0.1)	(0.1)	(0.0)	(0.0)	(0.4)
CI_Ref_22	MORB[1]	2000	−21.7	0.9	49.5	1.4	15.9	11.0	0.2	7.2	11.6	2.6	0.2	0.1	99.7
		(100)	(0.2)	(0.1)	(0.3)	(0.1)	(0.1)	(0.1)	(0.0)	(0.1)	(0.1)	(0.1)	(0.0)	(0.0)	(0.4)
CI_Ref_23	MORB[1]	2700	−27.7	1.2	49.6	1.4	15.9	11.0	0.2	7.1	11.4	2.6	0.2	0.1	99.6
		(400)	(0.2)	(0.1)	(0.2)	(0.1)	(0.1)	(0.2)	(0.0)	(0.1)	(0.2)	(0.1)	(0.0)	(0.0)	(0.3)
CI_Ref_25	MORB[1]	9000	−9.9	1.0	48.9	1.4	15.8	11.0	0.2	7.1	12.2	2.5	0.2	0.1	99.4
		(1000)	(0.2)	(0.1)	(0.3)	(0.1)	(0.1)	(0.1)	(0.0)	(0.1)	(0.2)	(0.2)	(0.0)	(0.0)	(0.3)
CI_Ref_27	MORB[1]	5300	−27.6	1.2	49.5	1.4	15.7	11.0	0.2	7.1	11.5	2.5	0.2	0.1	99.1
		(700)	(0.2)	(0.1)	(0.3)	(0.1)	(0.2)	(0.1)	(0.0)	(0.1)	(0.1)	(0.1)	(0.0)	(0.0)	(0.3)
CI_Ref_28	MORB[1]	9000	−27.3	1.4	49.1	1.3	15.8	11.0	0.2	7.1	11.4	2.6	0.2	0.1	98.8
		(900)	(0.2)	(0.1)	(0.2)	(0.1)	(0.2)	(0.2)	(0.0)	(0.1)	(0.1)	(0.1)	(0.0)	(0.0)	(0.3)

CI_bas_1	Basanite[1]	12000	−26.8	1.7	44.5	4.3	15.0	12.3	0.2	5.3	9.9	4.2	1.7	1.0	98.3
		(700)	(0.2)	(0.1)	(0.3)	(0.1)	(0.1)	(0.2)	(0.0)	(0.1)	(0.1)	(0.1)	(0.1)	(0.1)	(0.3)
CI_bas_2	Basanite[1]	3600	−25.6	1.7	44.8	4.3	15.0	12.4	0.2	5.4	9.9	4.1	1.7	1.0	98.7
		(400)	(0.2)	(0.1)	(0.2)	(0.1)	(0.1)	(0.2)	(0.0)	(0.1)	(0.1)	(0.1)	(0.1)	(0.1)	(0.3)
CI_bas_3	Basanite[1]	5800	−1.1	1.5	44.5	4.2	15.0	12.0	0.2	5.5	10.2	4.1	1.8	0.9	98.4
		(700)	(0.2)	(0.2)	(0.5)	(0.1)	(0.3)	(0.1)	(0.0)	(0.1)	(0.3)	(0.2)	(0.1)	(0.1)	(0.5)
CI_bas_4	Basanite[1]	2200	−11.9	1.3	44.5	4.3	14.9	12.5	0.2	5.4	10.5	4.2	1.7	0.9	99.0
		(500)	(0.2)	(0.1)	(0.8)	(0.1)	(0.3)	(0.2)	(0.0)	(0.1)	(0.4)	(0.2)	(0.1)	(0.1)	(0.6)
CI_bas_5	Basanite[1]	1800	−8.6	1.6	44.7	4.2	15.0	12.3	0.2	5.3	10.3	4.1	1.8	1.0	98.8
		(200)	(0.2)	(0.1)	(0.5)	(0.1)	(0.2)	(0.2)	(0.0)	(0.1)	(0.3)	(0.2)	(0.1)	(0.1)	(0.5)
CI_bas_6	Basanite[1]	8400	−26.1	1.7	44.9	4.2	15.0	12.3	0.2	5.3	9.8	4.2	1.7	1.0	98.6
		(800)	(0.2)	(0.1)	(0.3)	(0.1)	(0.1)	(0.1)	(0.0)	(0.1)	(0.1)	(0.1)	(0.1)	(0.1)	(0.4)
CI_bas_7	Basanite[1]	3600	−14.5	1.3	44.4	4.3	14.9	12.4	0.2	5.4	10.4	4.2	1.7	1.0	98.8
		(400)	(0.2)	(0.1)	(0.8)	(0.1)	(0.2)	(0.3)	(0.0)	(0.1)	(0.4)	(0.2)	(0.1)	(0.1)	(0.9)
CI_bas_8	Basanite[1]	4100	−9.1	1.3	43.9	4.3	14.7	12.2	0.2	5.3	11.0	4.1	1.7	1.0	98.3
		(500)	(0.6)	(0.1)	(0.7)	(0.1)	(0.3)	(0.1)	(0.0)	(0.1)	(0.3)	(0.2)	(0.1)	(0.1)	(0.6)
CI_bas_9	Basanite[1]	7600	−13.0	1.1	44.0	4.3	14.7	12.6	0.2	5.4	10.5	4.2	1.7	1.0	98.6
		(800)	(0.2)	(0.3)	(0.5)	(0.1)	(0.2)	(0.1)	(0.0)	(0.1)	(0.3)	(0.2)	(0.1)	(0.1)	(0.6)
CI_AMNH_NBO_1_3	NBO[2]	800	−27.4	2.5	56.4	2.7	18.4	6.7	0.1	3.4	6.0	2.4	1.0	0.6	97.7
		(100)	(0.2)	(0.4)	(0.6)	(0.1)	(0.4)	(0.2)	(0.0)	(0.1)	(0.1)	(0.1)	(0.1)	(0.0)	(0.3)
CI_AMNH_NBO_2	NBO[2]	1000	−27.5	2.9	54.7	3.0	16.5	7.8	0.1	3.7	6.7	2.9	1.3	0.7	97.4
		(100)	(0.2)	(0.4)	(0.2)	(0.1)	(0.1)	(0.2)	(0.0)	(0.1)	(0.1)	(0.1)	(0.1)	(0.1)	(0.4)
CI_AMNH_NBO_3_1	NBO[2]	1400	−27.7	2.7	49.7	3.5	17.2	9.0	0.2	4.4	7.9	3.2	1.4	0.8	97.2
		(80)	(0.2)	(0.2)	(0.3)	(0.1)	(0.1)	(0.1)	(0.0)	(0.1)	(0.1)	(0.1)	(0.1)	(0.1)	(0.6)
CI_AMNH_NBO_4	NBO[2]	1900	−27.0	2.3	47.7	3.9	15.7	10.2	0.2	4.8	8.7	3.6	1.6	0.8	97.2
		(300)	(0.2)	(0.1)	(0.3)	(0.1)	(0.1)	(0.1)	(0.0)	(0.1)	(0.1)	(0.1)	(0.1)	(0.1)	(0.4)
DR52	Test (DR52[3])_	380	−8.2	0.1	50.3	1.4	16.7	10	0.2	8.9	11.1	3.0	0.1	0.1	101.8
		(40)	(0.2)	(0.0)	(0.3)	(0.1)	(0.1)	(0.1)	(0.0)	(0.1)	(0.1)	(0.1)	(0.0)	(0.0)	(0.5)
ETNA3−2	Test (ETNA[2])	3300	−22.7	2.7	47.9	1.6	16.3	9.7	0.2	6.3	10.5	3.2	1.9	0.5	98.1
		(100)	(0.2)	(0.1)	(0.2)	(0.1)	(0.1)	(0.1)	(0.0)	(0.1)	(0.1)	(0.2)	(0.1)	(0.0)	(0.4)
ETNA3−2bis	Test (ETNA[2])	3340	−22.2	2.8	47.8	1.6	16.0	10.4	0.2	6.2	10.3	3.2	1.8	0.5	98.1
		(50)	(0.2)	(0.1)	(0.2)	(0.1)	(0.1)	(0.1)	(0.0)	(0.1)	(0.1)	(0.1)	(0.1)	(0.0)	(0.3)
ETNA3−3	Test (ETNA[2])	3600	−24.2	1.7	48.9	1.6	16.2	9.8	0.2	6.3	10.6	3.3	1.9	0.6	99.3
		(200)	(0.2)	(0.1)	(0.6)	(0.1)	(0.2)	(0.3)	(0.0)	(0.1)	(0.1)	(0.1)	(0.1)	(0.0)	(0.3)
CI_IPGP_B6	Test (Hawaii[2])	1900	−28.1	1.5	49.5	2.1	11.6	12.0	0.2	11.8	9.8	1.9	0.4	0.2	99.5
		(400)	(0.2)	(0.1)	(0.2)	(0.1)	(0.2)	(0.1)	(0.0)	(0.3)	(0.1)	(0.1)	(0.1)	(0.0)	(0.3)

[1] This study

[2] Lee et al. (2024)

[3] Maevaray, (2017)

307

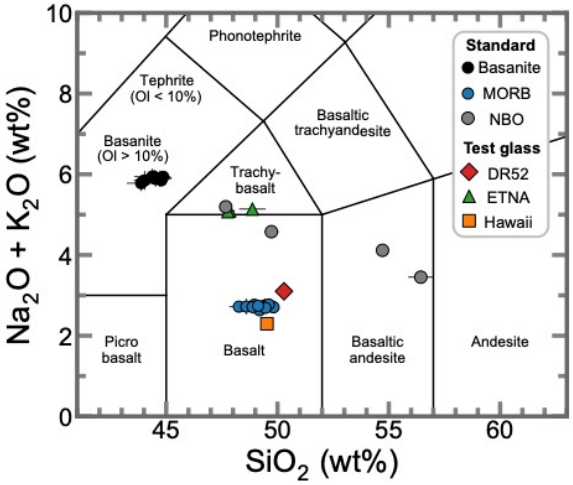

Fig. 1 Total alkali versus silica diagram showing the composition of the standards and test glasses.

3.1.2. Volatile concentrations

Standard glasses range in CO_2 concentrations from 1800±200 to 12000±700 ppm (Fig. 2 and Table 1). Specifically, the CO_2 concentrations of the MORB series range from 2000±100 to 9200±400 ppm, while the Basanite series has a wider range, covering values from 1800±200 to 12000±700 ppm. The range of H_2O concentrations is relatively limited, with average values of 1.3 wt% including both the MORB and Basanite series, ranging from 0.8±0.1 to 1.7±0.1 wt%. The NBO series has a lower range of CO_2 concentration than MORB and Basanite, ranging from 800±100 to 1900±300 ppm. H_2O content of NBO series is higher than the MORB and Basanite, ranging from 2.3±0.1 to 2.9±0.4 wt%. The errors in CO_2 and H_2O measurements were estimated as the standard deviation (1σ) of 3 to 9 repeated FTIR analyses, as shown in Table 1.

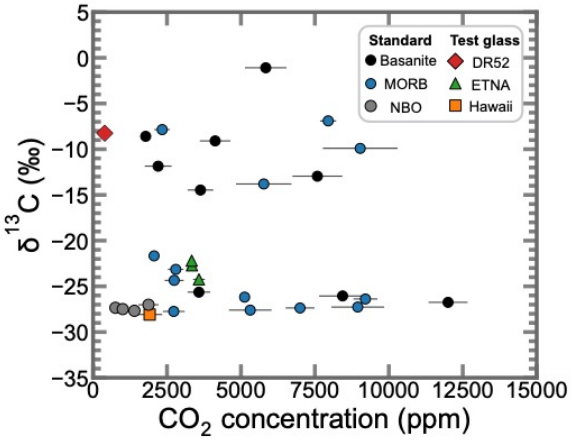

Fig. 2: $\delta^{13}C$–value versus CO_2 content of standard and test glasses. X–axis shows CO_2 concentration measured by FTIR. The error bar represents the standard deviation on 3 to 9

repeated analyses. Y–axis shows the $\delta^{13}C$–value measured by EA–IRMS and the error bar represents either the analytical error (0.2 ‰) or the standard deviation on repeated analysis (see 3.1.3 for details) but are all smaller than the symbols.

3.1.3. $\delta^{13}C$–value by EA-IRMS

The $\delta^{13}C$–values of the standards range from –1.1±0.2 to –28.1±0.2 ‰ (Fig. 2 and Table 1). The MORB series, $\delta^{13}C$–values range from –6.9±0.3 ‰ to –27.7±0.2 ‰, and the Basanite series from –1.1±0.2 ‰ to –26.8±0.2 ‰. The NBO series is characterized by a more limited range of $\delta^{13}C$–values, ranging from –27.0±0.2 ‰ to –27.7±0.2 ‰. Due to the limited amount of sample and the destructive nature of the analyses only 10 standards were measured multiple times. For samples that were measured twice, the error was assessed by calculating the standard deviation of the repeated measurements (1σ), which ranged from ±0.2 ‰ to ±0.6 ‰ (average ±0.2 ‰). Samples analyzed only once were assigned an error estimated from the analytical error of the EA–IRMS which is ±0.2 ‰.

3.2. $\delta^{13}C$–value analysis by SIMS

3.2.1. Precision and homogeneity

The internal precision for $\delta^{13}C$−value measurements performed by SIMS including both standards and test glasses, represented by the standard deviation of the mean (1σ) of each analysis, ranged from ±0.5 to ±1.9 ‰ (avg. ±0.7 ‰) on the Nancy IMS 1270 and from ±0.6 to ±1.7 ‰ (avg. ±1.1 ‰) on the WHOI IMS 1280. Notably, the internal precision improved significantly with increasing ^{12}C and ^{13}C counts (Fig. 3). Beyond 200,000 cps on ^{12}C and 2,000 cps on ^{13}C, the internal precision mostly improved to less than ±1.0 ‰ for both instruments. Thus, optimization of primary beam intensity and analytical conditions to maximize ^{12}C and ^{13}C counts is critical to achieve high internal precision.

External precision, also called reproducibility or repeatability, is represented by the standard deviation on repeated analyses. The external precision was calculated from the standard deviation (1σ) of the instrumental mass fractionation (IMF) corrected $\delta^{13}C$−value (see 3.2.3 for detailed correction). In both the WHOI and Nancy instruments, the average reproducibility of $\delta^{13}C$−value was ±0.9 ‰ for Nancy (ranging from ±0.4 to ±2.4 ‰) and ±1.0 ‰ for WHOI (ranging from ±0.3 to ±2.7 ‰) (Table 2). In theory, the external precision and the average internal precision for a series of analyses of an isotopically homogeneous sample should be equivalent. The isotopic

357 homogeneity of the standards was supported by the similarities of external and internal precision
358 values (0.3 ‰ and 0.4 ‰ average difference for Nancy and WHOI, respectively; Table 2 and Fig.
359 4).

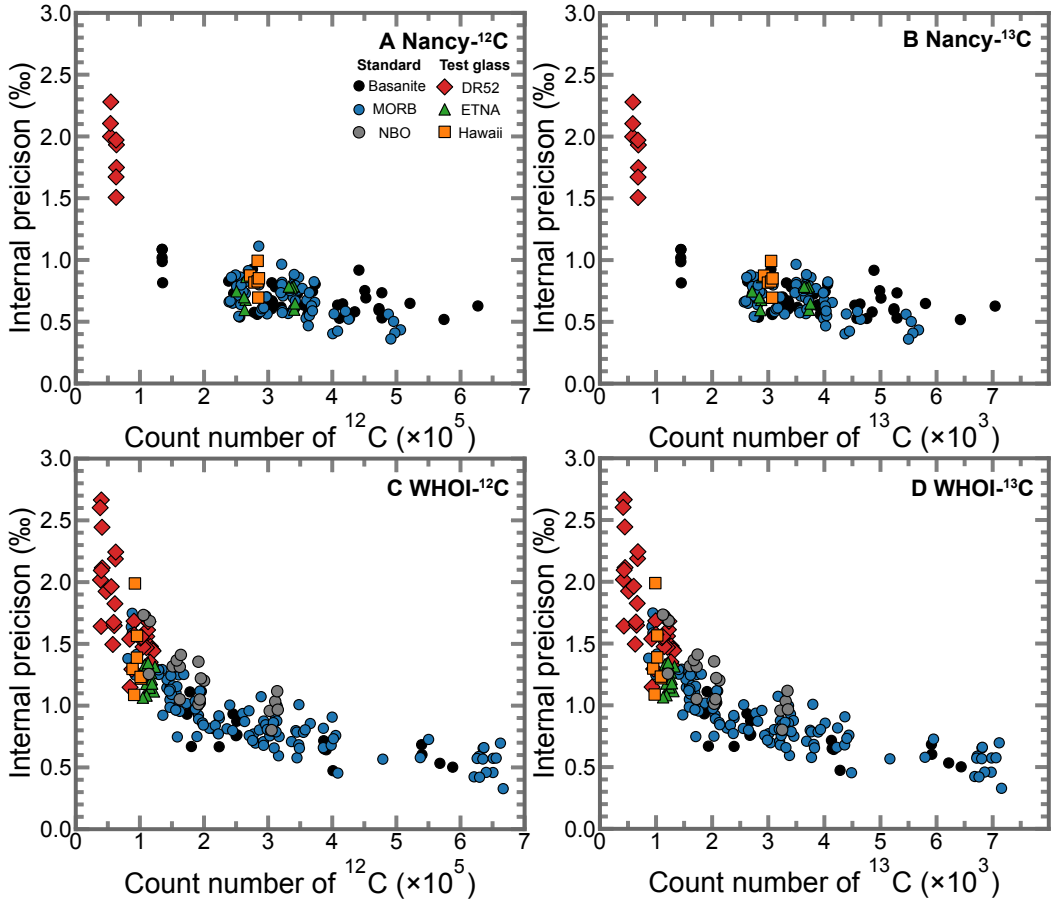

360

361 **Fig. 3** Internal precision (in ‰) versus counts per second (cps) of ^{12}C and ^{13}C in the axial electron
362 multiplier (EM). (A) and (B) shows ^{12}C and ^{13}C results obtained on the Ion Microprobe in Nancy,
363 while (C) and (D) shows ^{12}C and ^{13}C results obtained on the Ion Microprobe in WHOI, respectively.
364 Both sets of results show that the precision improves as the count rate of ^{12}C and ^{13}C increases. In
365 particular, the precision is better than ±1.0 ‰ above 200,000 cps on ^{12}C and 2,000 cps on ^{13}C.

366

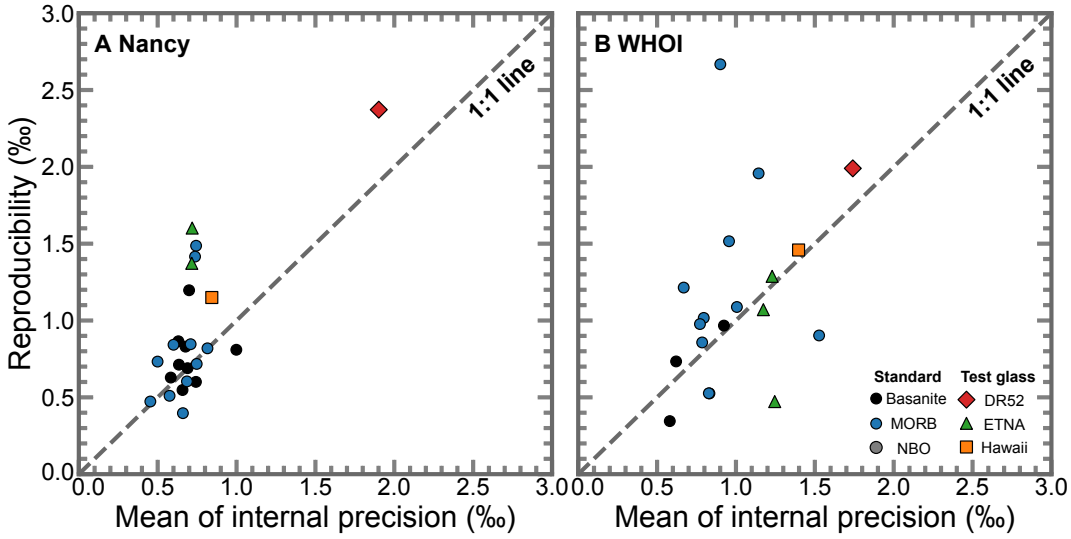

Fig. 4 Internal versus external precision for results obtained at (A) Nancy and (B) WHOI. The x–axis represents the average internal precision in permil (‰) for repeated measurements on the same glass chips, while the y–axis represents the external reproducibility, indicated by the standard deviation of the IMF corrected $\delta^{13}C$–values. Ideally, a homogeneous sample would have identical internal and external precision. The dashed line represents a 1:1 relationship.

Table 2

Summary of internal precision (1σ) and external precision (1σ) from Nancy and WHOI in permil (‰)

Name	Type	Number of measurements	Internal precision	External precision	Number of measurements	Internal precision	External precision
		Nancy			WHOI		
CI_Ref_4	MORB				4	0.8	0.5
CI_Ref_6	MORB	5	0.7	0.6	8	1.0	1.1
CI_Ref_9	MORB	5	0.6	0.5	4	0.8	1.0
CI_Ref_10	MORB	5	0.8	0.7	8	0.8	1.0
CI_Ref_11	MORB	5	0.5	0.7	4	0.8	0.9
CI_Ref_18	MORB	5	0.6	0.8	37	0.9	2.7
CI_Ref_22	MORB	5	0.7	1.5	8	1.0	1.5
CI_Ref_23	MORB	5	0.7	0.9			
CI_Ref_25	MORB	5	0.8	0.8	8	1.1	2.0
CI_Ref_15	MORB	6	0.8	0.8	7	1.5	0.9
CI_Ref_20	MORB	5	0.5	0.5			

CI_Ref_27	MORB	5	0.7	0.4	24	0.7	1.2
CI_Ref_28	MORB	5	0.7	1.4			
CI_bas_1	Basanite	5	0.7	0.6	4	0.6	0.7
CI_bas_2	Basanite	5	0.7	0.8	9	0.9	1.0
CI_bas_3	Basanite	5	0.7	0.6	4	0.6	0.4
CI_bas_4	Basanite	5	0.6	0.7			
CI_bas_5	Basanite	5	0.7	1.2			
CI_bas_6	Basanite	5	1.0	0.8	4	0.8	0.5
CI_bas_7	Basanite	5	0.7	0.7			
CI_bas_8	Basanite	5	0.6	0.6			
CI_bas_9	Basanite	5	0.6	0.9			
CI_AMNH_NBO_1_3	NBO				4	1.6	0.5
CI_AMNH_NBO_2	NBO				5	1.3	0.3
CI_AMNH_NBO_3_1	NBO				5	1.2	1.0
CI_AMNH_NBO_4	NBO				5	1.0	0.3
DR52	Test (DR52)_	8	1.9	2.4	33	1.7	2.0
ETNA3−2	Test (ETNA)	5	0.7	1.4	5	1.2	1.1
ETNA3−2bis	Test (ETNA)				3	1.3	0.5
ETNA3−3	Test (ETNA)	5	0.7	1.6	8	1.2	1.3
CI_IPGP_B6	Test (Hawaii)	6	0.8	1.2	7	1.4	1.5

3.2.2. IMF and drift

To ensure accurate results, it is imperative to calibrate the instrumental mass fractionation (IMF) and address any potential drift. IMF can be expressed in either α or δ notation, as described by eq.1 and eq.2, when $R = {}^{13}C/{}^{12}C$, $R_{measured}$ is the raw ratio measured by SIMS, and R_{true} is what we measured from EA−IRMS.

$$\text{IMF } (\alpha) = \frac{R_{measured}}{R_{true}} \quad \text{eq. 1}$$

$$\text{IMF } (‰) = \left(\frac{R_{measured}}{R_{true}} - 1\right) \times 1000 \quad \text{eq. 2}$$

IMF is due to the preferential ionization of lighter isotopes relative to heavier ones during secondary ion emission (e.g., Slodzian et al., 1980). This results in a depletion of the measured SIMS isotope ratios for heavier isotopes compared to the true ratio (e.g., De Hoog and EIMF, 2018; Hartley et al., 2012; Hauri et al., 2006). The extent of depletion depends on a number of factors, including instrument type, sample location, temporal drift, analytical configuration, primary beam intensity, and matrix composition effects.

Significant differences in IMF were observed between different facilities and setups at Nancy (ranges from α =0.955 to 0.971, avg. 0.963) and WHOI (ranges from α =0.968 to 0.989, avg. 0.980). We divided the WHOI session into five sub−sessions where different analysis conditions were used (Fig. 5). In the second session at WHOI, the mount was rotated 90 degrees and reinserted, and there was no systematic variation in IMF before and after reinsertion. In the third session at WHOI, the mount was reinserted, and a drift in IMF over time was characterized. However, in the fifth session at WHOI, DR52 analysis was inserted every 5 measurements, which showed no systematic drift over time. In the fourth and fifth sessions at WHOI, different analysis parameters from the first three sessions were attempted to reduce the background. The background was reduced by 10 % by increasing the pre–sputter grid size from 15 µm to 20 µm, increasing the pre–sputter time from 120 to 300 seconds, and reducing the field aperture (from 3000 µm to 1500 µm) and exit slit (from 303 µm to 243 µm). However, this also affected the IMF by more than 2 ‰.

A negative correlation between IMF and primary beam intensity (in the range of 0.2 – 2.2 nA) was observed only in the Basanite series analyzed at Nancy (Fig. 6A). A linear regression calibration between beam intensity and IMF was performed to account for this variability. In the MORB series at Nancy (in the range of 0.5 – 2.4 nA) (Fig. 6B) and in all series at WHOI, no such correlation was observed. The effect of matrix composition on the IMF is discussed further in Section 4.5.

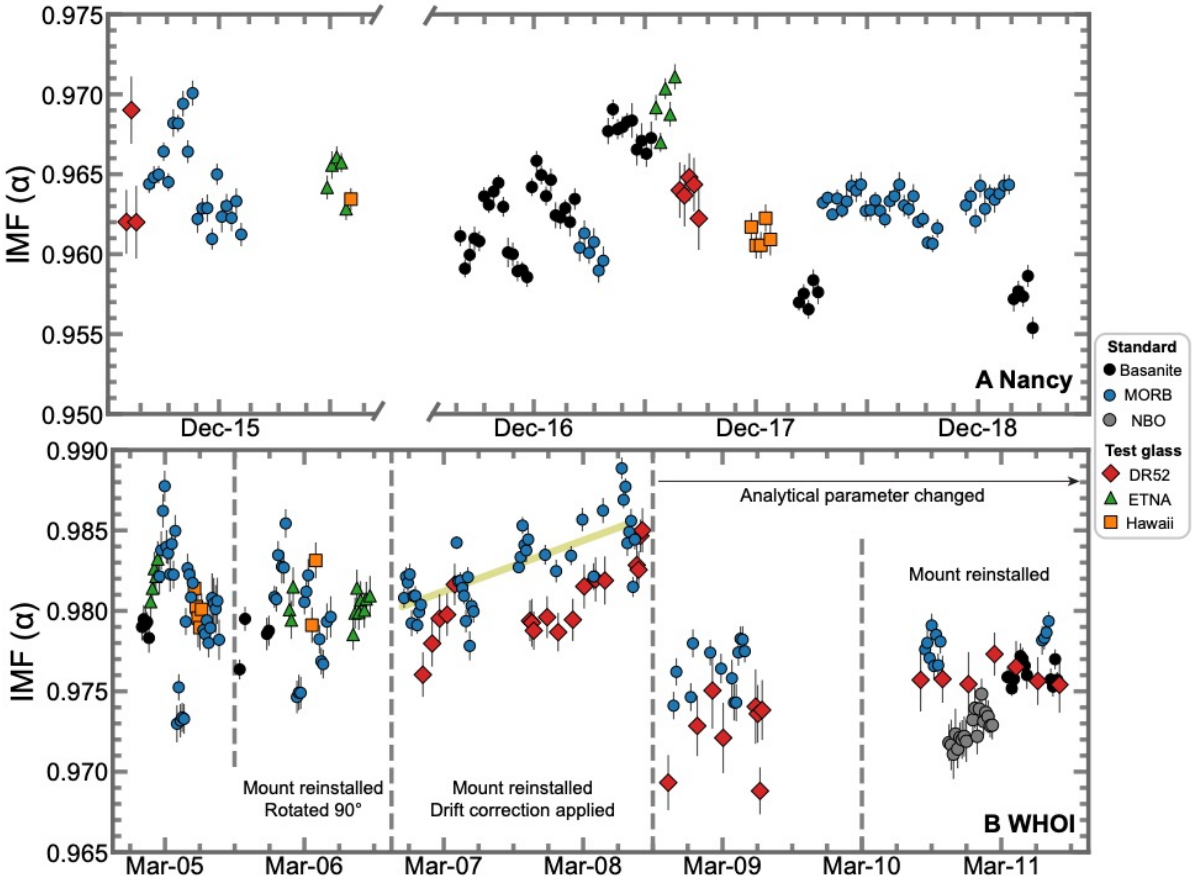

Fig. 5 Estimated IMF (in alpha) between raw $R_{measured}$ and R_{true} measured by EA–IRMS as a function of time during the (A) Nancy and (B) WHOI session. For Nancy, the x−axis is broken where there is no data. For WHOI session, the dashed line separates each sub−session, from the first to the fifth. From the first to the second session the mount was reinstalled with a 90–degree rotation, resulting in IMF values comparable to the first session. In the third session, a drift over time was observed after the mount reinstallation, with the green line representing a linear regression of the MORB standards used to track the drift. IMF changes occurred from the fourth session due to changes in analytical parameters (see 3.2.2 for details). In the fifth session, DR52 was analyzed every 5 measurements and showed no systematic drift over time.

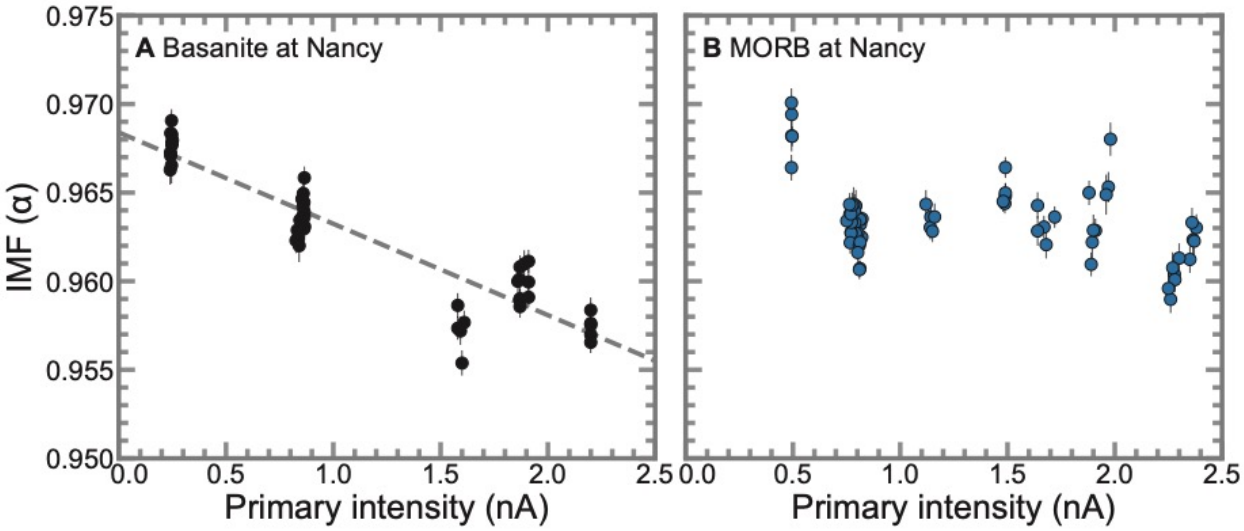

Fig. 6 Comparison between IMF in alpha and primary intensity in nA in the Nancy session (A) for Basanite standard sets and (B) for MORB standard sets. The dashed line in (A) represents the linear regression line.

3.2.3. Accuracy and correction

For the final IMF correction, we generally used the average IMF obtained from appropriate compositional standards. Synthetic glasses (Etna, Hawaii) and natural MORB (DR52) are used as unknowns to validate the IMF correction. The test glasses were corrected using the IMF determined from the MORB series due to their compositional proximity to MORB.

At Nancy, the average of the IMF of the MORB series was used to correct the $R_{measured}$ values for the MORB series and the test glasses. For the Basanite standards, a linear regression between primary beam intensity and IMF was used to correct $R_{measured}$. At WHOI, since the first and second sessions showed consistent IMF (Fig. 5), we used the average value from these two sessions. In the third session, a drift correction to the IMF was applied by performing a linear regression on the MORB standards over time. Finally, we used the average value from the fourth and fifth sessions to calculate the IMF during that time.

The IMF−corrected $\delta^{13}C$–values are presented in Fig. 7. There was a notable agreement between the $\delta^{13}C$–value measured by EA–IRMS and SIMS down to ~380 ppm CO_2 (DR52).

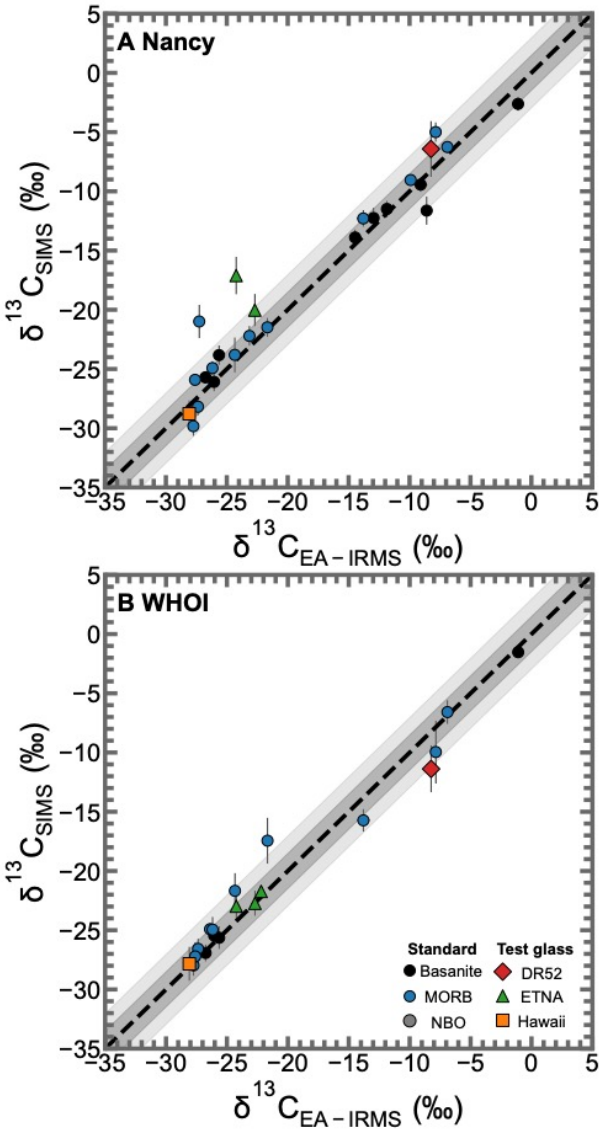

Fig. 7 Comparison between "true" $\delta^{13}C$–value measured by EA−IRMS (x−axis) and IMF–corrected $\delta^{13}C$–value measured by SIMS (y−axis). The dashed line is the 1:1 line. Around the dashed lines, two areas of different shading represent 1σ and 2σ errors, respectively. Note that the IMF correction is specific for the Basanite and MORB series. The MORB IMF was used for the test glasses (all of basaltic composition). The error bar is 1σ for both axes.

3.3. CO_2 concentration calibration

To estimate CO_2 concentration by SIMS, we calibrated the $^{12}C/^{18}O$ ratio with the CO_2 concentrations determined by FTIR (Fig. 8). Calibration slopes were found to be consistent across the MORB and Basanite series. The systematic deviation of the NBO series (basalt to andesitic basalt) from the calibration line could be due either to the matrix effect (different matrix

composition between Basanite/MORB series and NBO series) or to the use of different FTIR absorption coefficients (Shishkina et al., 2014 for Basanite/MORB series; Dixon and Pan, 1995 for NBO series). The resulting calibration showed linearity over a wide range of CO_2 abundances (370 to 12000 ppm). SIMS 1−sigma error on the regressions are ±24 % for the Nancy session and ±21 % for the WHOI session, while the average error (1σ) on the FTIR CO_2 measurements is ± 11 %.

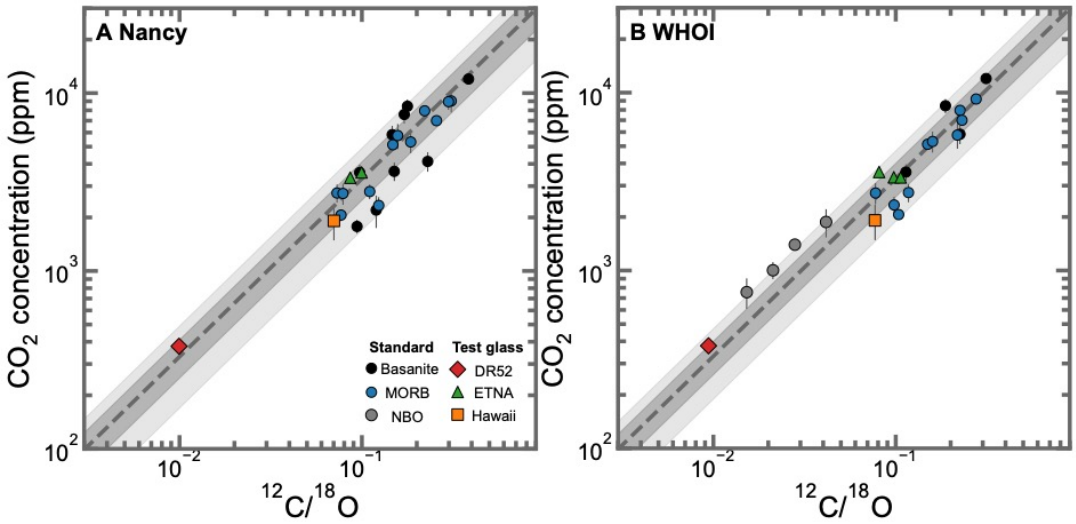

Fig. 8 $^{12}C/^{18}O$ ratio determined by SIMS at Nancy (A) and WHOI (B) versus CO_2 concentration in parts per million (ppm) measured by FTIR, except for DR52, which is measured by the step−heating method. Dashed lines are linear regression estimated in lienar−linear space. Around the dashed lines, two differently shaded areas indicate 1σ and 2σ percent error estimated in linear−linear space. The intercept of the linear regression was forced to zero.

4. Discussion

4.1. IMF and analytical conditions

This study investigated interlaboratory reproducibility by performing analyses on ion microprobe instruments at Nancy (IMS 1270) and WHOI (IMS 1280). Significant differences in IMF were found between the two instruments. Several important differences may help explain the large variations in IMF. The labs have different large−geometry SIMS models: IMS 1270 at Nancy and IMS 1280 at WHOI. Although we used EM detectors on both SIMS, the Nancy session was performed in mono–collector mode with peak switching for ^{12}C and ^{13}C, while the WHOI session was performed in dynamic multi–collector mode.

Another factor contributing to the variation in IMF is the adjustment of the analytical parameters. One of the main reasons for IMF is the non−uniform distribution of secondary ions of different masses in a constant magnetic field, such as the Earth's magnetic field (e.g., Sangely et al., 2014). As a result, mechanical obstacles along the path of the secondary ions, such as entrance slits or field apertures, intercept only a portion of the heterogeneous secondary beam. This selective interception inevitably leads to deviations in the measured isotopic ratio from the natural distribution of the respective isotopes. In the fourth and fifth sub−sessions at WHOI, different analytical parameters were attempted than in the first three sub−sessions. The main parameter changes were the reduction of the field aperture and the exit slit (see 2.4.3 for details), which resulted in IMF shifts of more than 2 ‰. We also suspect that the opening of the field aperture up to 3000 μm in the first three sub−sessions shows more scattered IMF (Fig. 5) compared to the last two sub−sessions due to the high background.

4.2. IMF and sample location on the mount

The collection efficiency of secondary ions is affected by the position of the sample in the holder. The study of oxygen isotope on silicon wafer (Goldstein et al., 1993) indicates that reliable results can be obtained even when the sample is close to the edge of the holder as long as the analysis spot is close to the center of the sample. Nonetheless, it is recommended that extreme edge positions in the holder should be avoided. In our study, standard mounts were well–centered in the sample holder to avoid edge positions (Fig. S2).

To test the possible effect of the position of the sample in the sample holder on the IMF (e.g., Fàbrega et al., 2017), we performed two sets of analyses on the same standards before and after rotating the sample holder 90 degrees (sub−sessions 1 and 2 at WHOI). We found no systematic variation in IMF before and after the rotation (Fig. 5) indicating that sample position within the holder has no measurable effect on the IMF.

4.3. IMF and primary beam intensity

Variations in the primary beam current result in variable beam densities and sputtering rates, which affect the surface ionization efficiency. For instance, an increase in IMF with primary beam intensity was reported for hydrogen isotopes in silicate glass (e.g., Hauri et al., 2006).

We explored a range of beam intensities from 0.5 to 2.4 nA on the Nancy IMS 1270 and found that, for the MORB series, there was no change in IMF with beam intensity (Fig. 6). For the Basanite series, however, we found a clear (R^2=0.85) correlation between beam intensity and IMF (Fig. 6A). One suspect for this correlation was a misestimation of the deadtime since the deadtime is count rate dependent for ^{12}C and count rate is itself dependent on C content. Incorrect estimation of the deadtime could create an artifact resulting in a positive correlation between primary intensity and IMF. Therefore, in Nancy, we were careful to recalculate the deadtime at the beginning of the session. The reason the Basanite series would show a shift in IMF with beam intensity while the MORB doesn't, over the same range of beam intensity, is unclear but further underscores the importance of using matrix−matched standards for this type of analysis.

4.4. Drift in IMF over time

Although drift in IMF on short timescales is not always observed (Fitzsimons et al., 2000), it commonly occurs for numerous elements and matrices (e.g., Eiler et al., 1997; Hauri et al., 2006; Taracsák et al., 2021). With the exception of the third sub−session at WHOI, the other sub−sessions at WHOI and the Nancy session showed no systematic drift in IMF over time. The third sub−session at WHOI showed a gradual increase in IMF. Frequent high–voltage adjustments to the detectors to maintain the pulse–height distribution curve can mitigate the IMF drift (e.g., Hedberg et al., 2015), which we applied to WHOI analyses. However, it is recommended that drift should be monitored by inserting standard analyses at regular intervals during the measurements, as well as at the beginning and end of the analytical session.

4.5. IMF and glass composition

Across various isotopes, the IMF in silicate glasses has been observed to vary as a function of compositional indices, for example, SiO_2 wt% (De Hoog and EIMF, 2018 for Li; Dubinina et al., 2021, Gurenko et al., 2001, Hartley et al., 2012 for O), H_2O and Al_2O_3 abundances (Haurie et al., 2006; Sobolev et al., 2019), SiO_2, Al_2O_3 and K_2O moles (Manzini et al., 2017 for Cl). To further explore the variation in IMF of carbon isotope across matrix compositions, we examined the Basanite and NBO series, which provide a range of compositions from basanite to basaltic andesite (Fig. 1). Table 3 was generated to show correlation coefficients of different compositional parameters with IMF.

IMF shows a negative correlation with mole fractions of SiO_2, Al_2O_3, and H_2O, while other cations show a positive correlation. This relationship may be due to differences in the efficiency of kinetic energy transfer from primary to secondary ions depending on the matrix composition (Eiler et al., 1997; Hauri et al., 2006). Efficient energy transfer in heavier matrices results in less fractionation from the true $^{13}C/^{12}C$ and hence higher IMF in alpha. CO_2 concentration in silicate glasses shows the lowest correlation with IMF, probably due to its insignificant effect on silicate glass density (Bourgue and Richet, 2001; Lange, 1994). This may also explain the negative correlation observed for lighter elements, especially H_2O. For H_2O, although H_2O is known to suppress carbon ionization in basaltic glass (e.g., Behrens et al., 2004; Moussallam et al., 2024; H_2O ranges 0.0–6.8 wt%), the limited H_2O range (0.8–1.7 wt% for MORB and Basanite series) in our study prevents confirmation of IMF variation with H_2O.

It remains challenging to determine the precise effects of individual elements on IMF due to limited data and compositional variations. Further detailed investigation of the relationship between IMF and composition is needed, however, underscoring the importance of selecting a standard that closely matches the composition of the sample of interest.

Table 3
Correlation and determination coefficient between various compositional indices and IMF in alpha for NBO series and Basanite results from WHOI. The list order is sorted from highest R^2 to lowest R^2.

Compositional index	Correlation coefficient (R)	Determination coefficient (R^2)
XFeO	0.88	0.77
XP_2O_5	0.88	0.77
X{Mg/(Mg+Fe)}	−0.87	0.76
Density (hydrous)	0.86	0.74
XNa_2O	0.85	0.72
XCaO	0.84	0.71
$XTiO_2$	0.84	0.7
NBO/T (hydrous)*	0.83	0.69
XMgO	0.83	0.69
Alkalinity	0.83	0.69
XH_2O	−0.83	0.69
$XSiO_2$	−0.82	0.67
XK_2O	0.81	0.65
XAl_2O_3	−0.73	0.53
XMnO	0.63	0.4
XCO_2	0.48	0.23

*calculated according to Iacono–Marziano et al. (2012)

551
552

4.6. Implication of this study

553
554 SIMS offers an advantage over bulk analysis for $\delta^{13}C$−value measurement by avoiding potential
555 contamination problems and allowing *in situ* analysis at the micron scale. Achieving smaller spots
556 with high precision is an imperative goal for the analysis of small objects such as melt inclusions.
557 While previous attempts have achieved reproducibility of 2–3 ‰ with a 40 μm primary beam
558 diameter at up to 50 nA (Hauri et al., 2002), such dimensions may not be suitable for all samples.
559 While higher beam intensities offer potentially higher precision, they also increase the beam
560 diameter and risk charging the sample surface. In particular, we would like to emphasize that in
561 our study, the precision levels typically below ±1.0 ‰ were achieved using a 10 μm diameter spot
562 size and less than 5 nA for CO_2 concentration down to 1800±200 ppm.
563

4.7. Recommendation for $\delta^{13}C$ analyses in silicate glasses by SIMS

564
565 All the standards presented here are available at the Ion Microprobe facility in CNRS−CRPG
566 Nancy for users there and will be deposited at the Smithsonian Museum of Natural History, where
567 they will be available to any researcher on request. Our recommendation for future analyses of
568 $\delta^{13}C$ in silicate glasses by SIMS is the following:

569 1. Reduce background: Mount samples in indium to reduce background interference from the
570 mount itself. Thoroughly clean off any crystal bond, acetone deposits, and other
571 contaminants in your samples before mounting them to minimize unwanted signals. Try to
572 obtain the best possible quality results at polishing. Cracks, cavities, caverns or any other
573 defects resulting from insufficient polishing usually contain rests of fiber and abrasive
574 materials and present a source of huge contamination by carbon that is nearly impossible to
575 eliminate by cleaning. In addition, it is recommended to use sufficient pre–sputtering time
576 for surface cleaning preparation to reduce background (120 seconds or more). However,
577 excessively long pre–sputtering or numerous analysis cycles should be avoided to prevent
578 targeting inaccurate location or uneven surface. Previous effort has used a 400 μm field
579 aperture to reduce background (Hauri et al., 2002), but this approach also attenuates the
580 signal as well. In our study, we reduced ^{12}C background intensity by a factor of 10 on the
581 olivine blank as a result of adjusting the field aperture size from 3000 μm to 1500 μm. It is

strongly recommended that background, which can be assessed using olivine (or any CO_2−free mineral) or devolatilized glass, be measured as blank at all analytical setups including beam currents throughout the session to keep track of carbon background contribution.

2. Optimize signal: As shown in Fig. 3, the higher the count rate, the better the precision. The relationship, however, is not linear such that very high−count rates (>300,000 cps on ^{12}C), liable to damage the detector are not recommended. Instead, it is recommended to aim for a count rate of around 300,000 cps on ^{12}C (3,000 cps on ^{13}C). To do so requires some *a priori* knowledge of the CO_2 content in the unknown glass in order to choose a beam current that would yield this count rate. It is also recommended to increase the count times or the number of cycles to achieve better precision, but too many analysis cycles should be avoided to avoid the same reasons as for too long pre−sputtering.

3. Characterize IMF in detail: We recommend analyzing multiple (at least five) standards of matrix−matched composition with your unknown in order to properly constrain the IMF during your analytical session. In addition, we recommend monitoring for drift by measuring the standards at the beginning and end of the session and/or by periodically performing repeated analysis on a standard during the session. Finally, if using multiple primary beam intensities on your unknown, we recommend testing the effect of this range of primary beam intensities on the standards of matrix−matched composition. The list of "best" standards, which are well characterized in both $\delta^{13}C$−values and CO_2 concentrations with nice homogeneity at Nancy or WHOI, is shown in Table S1.

5. Conclusion

In this study, we synthesized and characterized 31 experimental glasses of MORB and Basanite compositions intended to serve as international standards for $\delta^{13}C$−value measurements by SIMS. We achieved internal precision in the order of ±1.1 ‰ (minimum ±0.3 ‰) for spot sizes between 10 to 20 μm. This significant development makes possible the analysis of small samples such as melt inclusions. This precision was achieved by adjusting the primary beam intensity to maintain a ^{12}C signal around 300,000 cts/s. We demonstrated that our standards are homogeneous in $\delta^{13}C$–

values and allow characterization of instrumental mass fractionation (which can vary widely between instruments and analytical conditions) with an average reproducibility of ±1.0 ‰ for CO_2 concentration down to 1800±200 ppm. The reference glasses are now available at the CNRS–CRPG ion microprobe facility in Nancy and will be deposited at the Smithsonian National Museum of Natural History, where they will be freely available on loan to any researcher (*catalogue numbers will be available for the final version of this manuscript*).

Data availability

Raw analysis data are available through Mendeley Data at https://data.mendeley.com/preview/j6w5y8fsm3?a=b9f24828-80a9-4533-b979-eb9705f5297c.

Author contributions

Initial study design: H.L., Y.M.
Experiments: H.L., Y.M.
FTIR: H.L.
EA–IRMS: H.L.
EMPA: H.L.
SIMS (Nancy): Y.M., E.R.K., L.P., J.V., N.B., A.G., É.D.
SIMS (WHOI): H.L., Y.M., B.M., G.G.
Writing and interpretation: All authors, first draft H.L., Y.M.

Declaration of competing interest

The authors declare that they have no known competing financial interests or personal relationships that could have appeared to influence the work reported in this paper.

Declaration of generative AI in scientific writing

During the preparation of this work the authors used DeepL in order to improve readability and language. After using this tool, the authors reviewed and edited the content as needed and take full responsibility for the content of the publication.

Acknowledgment

Special thanks to Cyril Aubaud for providing the DR52 sample. We would also like to thank Céline Martin (AMNH) for her assistance with the microprobe analysis and Wei Huang for her valuable contributions to the analysis with the elemental analyser (LDEO). Funding: This work is part of Hyun Joo Lee's Ph.D. thesis, supported by the FORED (Foundation for Overseas Resources Development) scholarship program. We thank Marion Le Voyer for sharing her log−books and trial reports from 2012−2013, when she first started carbon isotope investigation by SIMS with Erik Hauri. Glenn Gaetani was supported by the *Independent Research & Development Program at WHOI.*

References

Barker, C., Torkelson, B.E., 1975. Gas adsorption on crushed quartz and basalt. Geochimica et Cosmochimica Acta 39, 212–218. https://doi.org/10.1016/0016-7037(75)90173-8

Barnes, J.D., Sharp, Z.D., 2006. Achlorine isotope study of DSDP/ODP serpentinized ultramafic rocks: Insights into the serpentinization process. Chemical Geology 228, 246–265. https://doi.org/10.1016/j.chemgeo.2005.10.011

Behrens, H., Ohlhorst, S., Holtz, F., Champenois, M., 2004. CO_2 solubility in dacitic melts equilibrated with H2O-CO2 fluids: Implications for modeling the solubility of CO_2 in silicic melts. Geochimica et Cosmochimica Acta 68, 4687–4703. https://doi.org/10.1016/j.gca.2004.04.019

Bourgue, E., Richet, P., 2001. The effects of dissolved CO_2 on the density and viscosity of silicate melts: a preliminary study. Earth and Planetary Science Letters 193, 57–68. https://doi.org/10.1016/S0012-821X(01)00491-5

Cartigny, P., Pineau, F., Aubaud, C., Javoy, M., 2008. Towards a consistent mantle carbon flux estimate: Insights from volatile systematics (H_2O/Ce, δD, CO_2/Nb) in the North Atlantic mantle (14°N and 34°N). Earth and Planetary Science Letters 265, 672–685. https://doi.org/10.1016/j.epsl.2007.11.011

Cocker, J.D., Griffin, B.J., Muehlenbachs, K., 1982. Oxygen and carbon isotope evidence for seawater-hydrothermal alteration of the Macquarie Island ophiolite. Earth and Planetary Science Letters 61, 112–122. https://doi.org/10.1016/0012-821X(82)90043-7

Craig, H., 1957. Isotopic standards for carbon and oxygen and correction factors for mass-spectrometric analysis of carbon dioxide. Geochimica et Cosmochimica Acta 12, 133–149. https://doi.org/10.1016/0016-7037(57)90024-8

De Hoog, J.C.M., EIMF, 2018. Matrix Effects During SIMS Measurement of the Lithium Mass Fractions of Silicate Glasses: Correction Procedures and Updated Preferred Values of Reference Materials. Geostandard Geoanalytic Res 42, 513–522. https://doi.org/10.1111/ggr.12237

Dixon, J.E., Pan, V., 1995. Determination of the molar absorptivity of dissolved carbonate in basanitic glass. American Mineralogist 80, 1339–1342. https://doi.org/10.2138/am-1995-11-1224

686 Dubinina, E., Borisov, A., Wiedenbeck, M., Rocholl, A., 2021. SIMS oxygen isotope matrix
687 effects in silicate glasses: Quantifying the role of chemical composition. Chemical
688 Geology 578, 120322. https://doi.org/10.1016/j.chemgeo.2021.120322
689 Eiler, J.M., Graham, C., Valley, J.W., 1997. SIMS analysis of oxygen isotopes: matrix effects in
690 complex minerals and glasses. Chemical Geology 138, 221–244.
691 https://doi.org/10.1016/S0009-2541(97)00015-6
692 Fàbrega, C., Parcerisa, D., Rossell, J.M., Gurenko, A., Franke, C., 2017. Predicting instrumental
693 mass fractionation (IMF) of stable isotope SIMS analyses by response surface
694 methodology (RSM). J. Anal. At. Spectrom. 32, 731–748.
695 https://doi.org/10.1039/C6JA00397D
696 Fitzsimons, I.C.W., Harte, B., Clark, R.M., 2000. SIMS stable isotope measurement: counting
697 statistics and analytical precision. Mineral. mag. 64, 59–83.
698 https://doi.org/10.1180/002646100549139
699 Goldstein, M., Chu, P.K., Bleiler, R.J., 1993. Determination of oxygen concentration in heavily
700 doped silicon. Journal of Vacuum Science & Technology B: Microelectronics and
701 Nanometer Structures Processing, Measurement, and Phenomena 11, 92–98.
702 https://doi.org/10.1116/1.586689
703 Gurenko, A.A., Chaussidon, M., Schmincke, H.-U., 2001. Magma ascent and contamination
704 beneath one intraplate volcano: evidence from S and O isotopes in glass inclusions and
705 their host clinopyroxenes from Miocene basaltic hyaloclastites southwest of Gran Canaria
706 (Canary Islands). Geochimica et Cosmochimica Acta 65, 4359–4374.
707 https://doi.org/10.1016/S0016-7037(01)00737-2
708 Hartley, M.E., Thordarson, T., Taylor, C., Fitton, J.G., Eimf, 2012. Evaluation of the effects of
709 composition on instrumental mass fractionation during SIMS oxygen isotope analyses of
710 glasses. Chemical Geology 334, 312–323. https://doi.org/10.1016/j.chemgeo.2012.10.027
711 Hauri, E., Wang, J., Dixon, J.E., King, P.L., Mandeville, C., Newman, S., 2002. SIMS analysis
712 of volatiles in silicate glasses. Chemical Geology 183, 99–114.
713 https://doi.org/10.1016/S0009-2541(01)00375-8
714 Hauri, E.H., Shaw, A.M., Wang, J., Dixon, J.E., King, P.L., Mandeville, C., 2006. Matrix effects
715 in hydrogen isotope analysis of silicate glasses by SIMS. Chemical Geology 235, 352–
716 365. https://doi.org/10.1016/j.chemgeo.2006.08.010
717 Hedberg, P.M.L., Peres, P., Fernandes, F., Renaud, L., 2015. Multiple ion counting measurement
718 strategies by SIMS – a case study from nuclear safeguards and forensics. J. Anal. At.
719 Spectrom. 30, 2516–2524. https://doi.org/10.1039/C5JA00382B
720 Iacono-Marziano, G., Morizet, Y., Le Trong, E., Gaillard, F., 2012. New experimental data and
721 semi-empirical parameterization of H_2O–CO_2 solubility in mafic melts. Geochimica et
722 Cosmochimica Acta 97, 1–23. https://doi.org/10.1016/j.gca.2012.08.035
723 Ihinger, P.D., Hervig, R.L., McMillan, P.F., 1994. Chapter 2. ANALYTICAL METHODS FOR
724 VOLATILES IN GLASSES, in: Carroll, M.R., Holloway, J.R. (Eds.), Volatiles in
725 Magmas. De Gruyter, pp. 67–122. https://doi.org/10.1515/9781501509674-008
726 Lange, R.A., 1994. Chapter 9. The effect of H_2O, CO_2 and F on the density and viscosity of
727 silicate melts, in: Carroll, M.R., Holloway, J.R. (Eds.), Volatiles in Magmas. De Gruyter,
728 pp. 331–370. https://doi.org/10.1515/9781501509674-015
729 Layne, G.D., Godon, A., Webster, J.D., Bach, W., 2004. Secondary ion mass spectrometry for
730 the determination of $\delta^{37}Cl$. Chemical Geology 207, 277–289.
731 https://doi.org/10.1016/j.chemgeo.2004.04.002

Lee, H.J., Moussallam, Y., Aubaud, C., Iacono-Marziano, G., Hammond, K., Ebel, D., 2024. Carbon isotope fractionation between CO_2 and carbon in silicate melts at high temperature. https://doi.org/10.31223/X5NH6R

Lesher, C.E., Spera, F.J., 2015. Thermodynamic and Transport Properties of Silicate Melts and Magma, in: The Encyclopedia of Volcanoes. Elsevier, pp. 113–141. https://doi.org/10.1016/B978-0-12-385938-9.00005-5

Loewen, M.W., Graham, D.W., Bindeman, I.N., Lupton, J.E., Garcia, M.O., 2019. Hydrogen isotopes in high $^3He/^4He$ submarine basalts: Primordial vs. recycled water and the veil of mantle enrichment. Earth and Planetary Science Letters 508, 62–73. https://doi.org/10.1016/j.epsl.2018.12.012

Longpré, M.-A., Stix, J., Klügel, A., Shimizu, N., 2017. Mantle to surface degassing of carbon- and sulphur-rich alkaline magma at El Hierro, Canary Islands. Earth and Planetary Science Letters 460, 268–280. https://doi.org/10.1016/j.epsl.2016.11.043

Maevaray, R., 2017. Caractérisation des éléments volatils dans une série de basaltes de ride de l'Océan Indien. Université Paris Diderot.

Manzini, M., Bouvier, A.-S., Barnes, J.D., Bonifacie, M., Rose-Koga, E.F., Ulmer, P., Métrich, N., Bardoux, G., Williams, J., Layne, G.D., Straub, S., Baumgartner, L.P., John, T., 2017. SIMS chlorine isotope analyses in melt inclusions from arc settings. Chemical Geology 449, 112–122. https://doi.org/10.1016/j.chemgeo.2016.12.002

Mathez, E.A., Delaney, J.R., 1981. The nature and distribution of carbon in submarine basalts and peridotite nodules. Earth and Planetary Science Letters 56, 217–232. https://doi.org/10.1016/0012-821X(81)90129-1

Mattey, D.P., 1991. Carbon dioxide solubility and carbon isotope fractionation in basaltic melt. Geochimica et Cosmochimica Acta 55, 3467–3473. https://doi.org/10.1016/0016-7037(91)90508-3

Mattey, D.P., Carr, R.H., Wright, I.P., Pillinger, C.T., 1984. Carbon isotopes in submarine basalts. Earth and Planetary Science Letters 70, 196–206. https://doi.org/10.1016/0012-821X(84)90005-0

Médard, E., Grove, T.L., 2008. The effect of H_2O on the olivine liquidus of basaltic melts: experiments and thermodynamic models. Contrib Mineral Petrol 155, 417–432. https://doi.org/10.1007/s00410-007-0250-4

Moussallam, Y., Georgeais, G., Rose-Koga, E.F., Koga, K.T., Hartley, M.E., Scaillet, B., Oppenheimer, C., Peters, N., 2023. CO_2 -Undersaturated Melt Inclusions From the South West Indian Ridge Record Surprisingly Uniform Redox Conditions. Geochem Geophys Geosyst 24, e2023GC011235. https://doi.org/10.1029/2023GC011235

Moussallam, Y., Longpré, M.-A., McCammon, C., Gomez-Ulla, A., Rose-Koga, E.F., Scaillet, B., Peters, N., Gennaro, E., Paris, R., Oppenheimer, C., 2019. Mantle plumes are oxidised. Earth and Planetary Science Letters 527, 115798. https://doi.org/10.1016/j.epsl.2019.115798

Moussallam, Y., Towbin, W., Plank, T., Bureau, H., Khodja, H., Guan, Y., Ma, C., Baker, M., Stolper, E., Naab, F., Monteleone, B., Gaetani, G., Lee, H.J., Ding, S., Shi, S., Rose-Koga, E., 2024. ND70 series basaltic glass reference materials for volatile element (H_2O, CO_2, S, Cl, F) analysis and the C ionisation efficiency suppression effect of water in silicate glasses in SIMS analysis. https://doi.org/10.31223/X5QQ4P

776 Nichols, A.R.L., Wysoczanski, R.J., 2007. Using micro-FTIR spectroscopy to measure volatile
777 contents in small and unexposed inclusions hosted in olivine crystals. Chemical Geology
778 242, 371–384. https://doi.org/10.1016/j.chemgeo.2007.04.007
779 Pineau, F., Javoy, M., 1983. Carbon isotopes and concentrations in mid-oceanic ridge basalts.
780 Earth and Planetary Science Letters 62, 239–257. https://doi.org/10.1016/0012-
781 821X(83)90087-0
782 Sakai, H., Casadevall, T.J., Moore, J.G., 1982. Chemistry and isotope ratios of sulfur in basalts
783 and volcanic gases at Kilauea volcano, Hawaii. Geochimica et Cosmochimica Acta 46,
784 729–738. https://doi.org/10.1016/0016-7037(82)90024-2
785 Sangely, L., Boyer, B., De Chambost, E., Valle, N., Audinot, J.-N., Ireland, T., Wiedenbeck, M.,
786 Aléon, J., Jungnickel, H., Barnes, J.-P., Bienvenu, P., Breuer, U., 2014. Secondary Ion
787 Mass Spectrometry, in: Prohaska, T., Irrgeher, J., Zitek, A., Jakubowski, N. (Eds.), Sector
788 Field Mass Spectrometry for Elemental and Isotopic Analysis. The Royal Society of
789 Chemistry, pp. 439–499. https://doi.org/10.1039/9781849735407-00439
790 Shimizu, K., Ushikubo, T., Murai, T., Matsu'ura, F., Ueno, Y., 2019. *In situ* analyses of
791 hydrogen and sulfur isotope ratios in basaltic glass using SIMS. Geochem. J. 53, 195–
792 207. https://doi.org/10.2343/geochemj.2.0559
793 Shishkina, T.A., Botcharnikov, R.E., Holtz, F., Almeev, R.R., Jazwa, A.M., Jakubiak, A.A.,
794 2014. Compositional and pressure effects on the solubility of H_2O and CO_2 in mafic
795 melts. Chemical Geology 388, 112–129. https://doi.org/10.1016/j.chemgeo.2014.09.001
796 Slodzian, G., Lorin, J.C., Havette, A., 1980. Isotopic effect on the ionization probabilities in
797 secondary ion emission. J. Phyique Lett. 41, 555–558.
798 https://doi.org/10.1051/jphyslet:019800041023055500
799 Sobolev, A.V., Asafov, E.V., Gurenko, A.A., Arndt, N.T., Batanova, V.G., Portnyagin, M.V.,
800 Garbe-Schönberg, D., Wilson, A.H., Byerly, G.R., 2019. Deep hydrous mantle reservoir
801 provides evidence for crustal recycling before 3.3 billion years ago. Nature 571, 555–559.
802 https://doi.org/10.1038/s41586-019-1399-5
803 Taracsák, Z., Neave, D.A., Beaudry, P., Gunnarsson-Robin, J., Burgess, R., Edmonds, M.,
804 Halldórsson, S.A., Longpré, M.-A., Ono, S., Ranta, E., Stefánsson, A., Turchyn, A.V.,
805 Eimf, Hartley, M.E., 2021. Instrumental mass fractionation during sulfur isotope analysis
806 by secondary ion mass spectrometry in natural and synthetic glasses. Chemical Geology
807 578, 120318. https://doi.org/10.1016/j.chemgeo.2021.120318
808 United States Geological Survey Reston Stable Isotope Laboratory, 2011, Report of Stable
809 Isotopic Composition Reference Material USGS41 (Carbon and Nitrogen Isotopes in L-
810 glutamic Acid), https://d9-wret.s3.us-west-
811 2.amazonaws.com/assets/palladium/production/s3fs-public/atoms/files/USGS41_0.pdf
812 (accessed 23 Apr 2024)
813 United States Geological Survey Reston Stable Isotope Laboratory, 2019a, Report of Stable
814 Isotopic Composition Reference Material USGS24 (Carbon Isotopes in Graphite),
815 https://d9-wret.s3.us-west-2.amazonaws.com/assets/palladium/production/s3fs-
816 public/media/files/USGS24.pdf (accessed 23 Apr 2024)
817 United States Geological Survey Reston Stable Isotope Laboratory, 2019b, Report of Stable
818 Isotopic Composition Reference Material USGS40 (Carbon and Nitrogen Isotopes in L-
819 glutamic Acid), https://d9-wret.s3.us-west-
820 2.amazonaws.com/assets/palladium/production/s3fs-public/atoms/files/USGS40_0.pdf
821 (accessed 23 Apr 2024)

Supplementary Material

High–precision determination of carbon stable isotope in silicate glasses by secondary ion mass spectrometry: Evaluation of international standards

Hyunjoo Lee[a,*], Yves Moussallam[a,b], Estelle F. Rose−Koga[c], Laurette Piani[d], Johan Villeneuve[d], Nordine Bouden[d], Andrey A. Gurenko[d], Brian Monteleone[e], Glenn A. Gaetani[e]

[a] *Lamont−Doherty Earth Observatory, Columbia University, New York, USA*

[b] *American Museum of Natural History, Department of Earth and Planetary Sciences, NY 10024, New York, USA*

[c] *ISTO, UMR 7327, Université d'Orléans−CNRS−BRGM, 1A rue de la Férollerie, 45071 Orléans cedex 2, France*

[d] *Centre de Recherches Pétrographiques et Géochimiques (CRPG), UMR 7358, CNRS-UL 15 rue Notre Dame des Pauvres, 54500 Vandœuvre-lès-Nancy, France*

[e] *Dept Geology and Geophysics, Woods Hole Oceanographic Institution, Woods Hole, MA 02543, USA*

Corresponding author: Hyunjoo Lee; hl3507@columbia.edu

Supplementary Figures

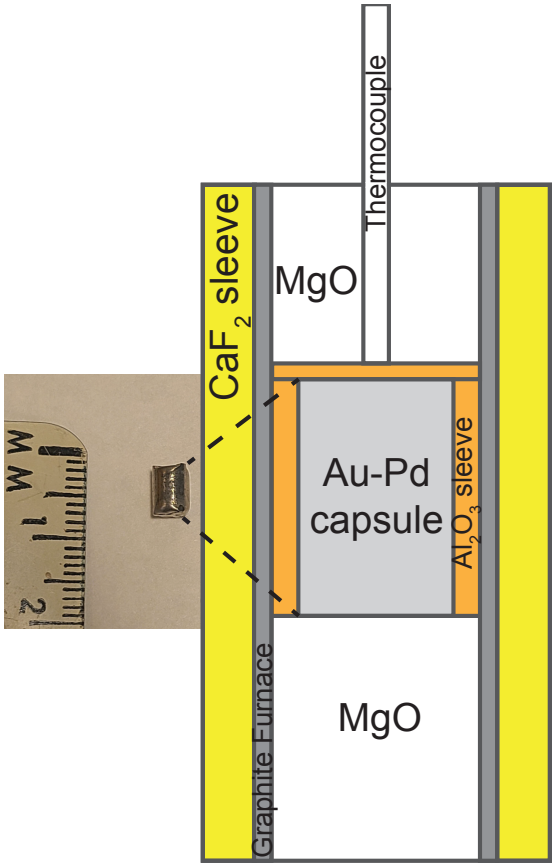

Fig. S1. Schematic diagram of the assembly used in the piston-cylinder experiment. Left picture shows the flattened final capsule of about 6 mm length before the experiment. The filled Au_{80}–Pd_{20} capsule was centered in a cylindrical graphite furnace with a high density Al_2O_3 sleeve and MgO spacers. The pressure medium was cylindrical CaF_2. A D-type thermocouple ($W_{97}Re_3$–$W_{75}Re_{25}$) was separated from the capsule by a 1 mm thick Al_2O_3 wafer.

A Nancy

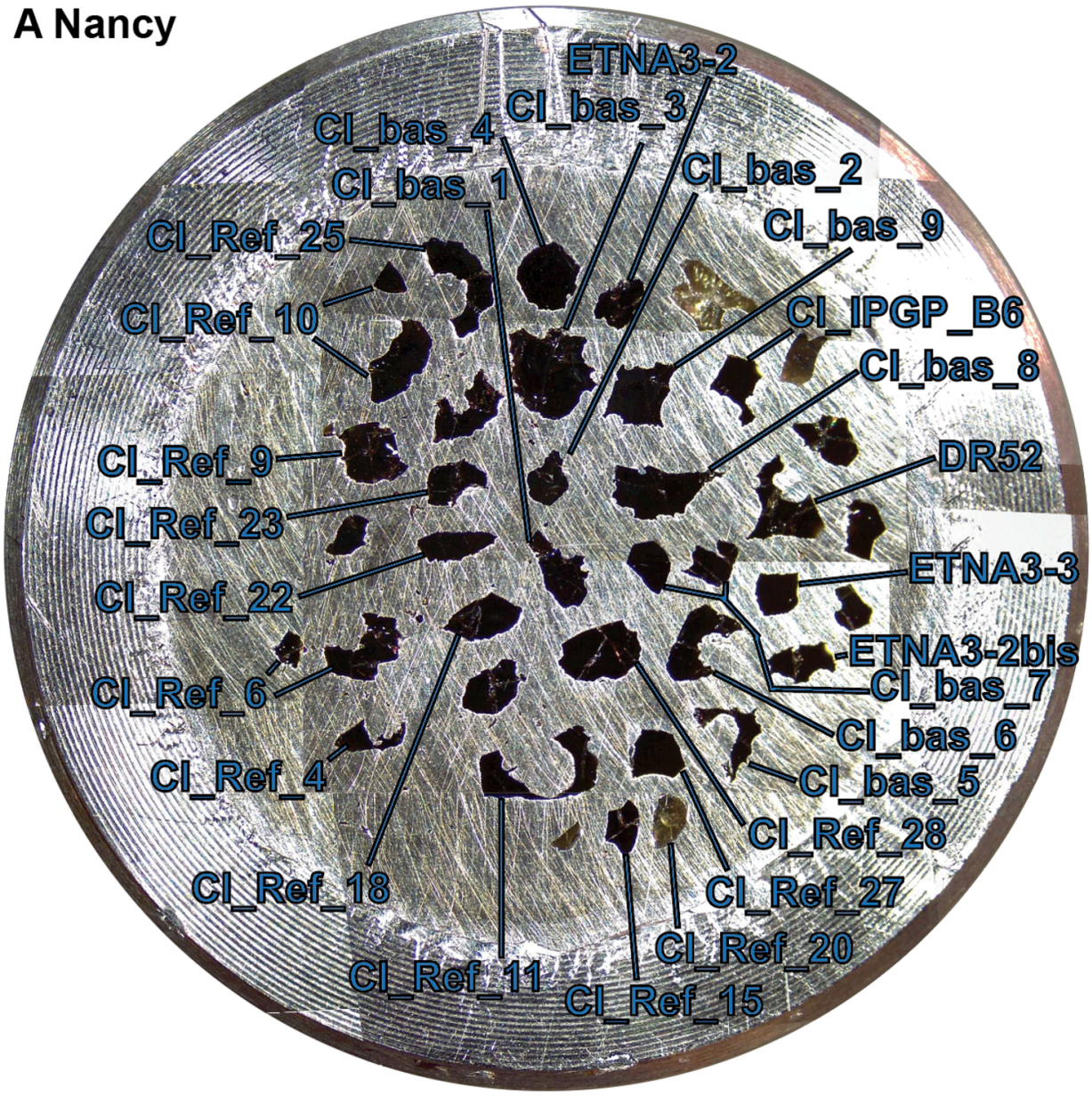
ETNA3-2
Cl_bas_3
Cl_bas_4
Cl_bas_1
Cl_bas_2
Cl_Ref_25
Cl_bas_9
Cl_Ref_10
Cl_IPGP_B6
Cl_bas_8
Cl_Ref_9
DR52
Cl_Ref_23
ETNA3-3
Cl_Ref_22
ETNA3-2bis
Cl_bas_7
Cl_Ref_6
Cl_bas_6
Cl_Ref_4
Cl_bas_5
Cl_Ref_28
Cl_Ref_18
Cl_Ref_27
Cl_Ref_20
Cl_Ref_11
Cl_Ref_15

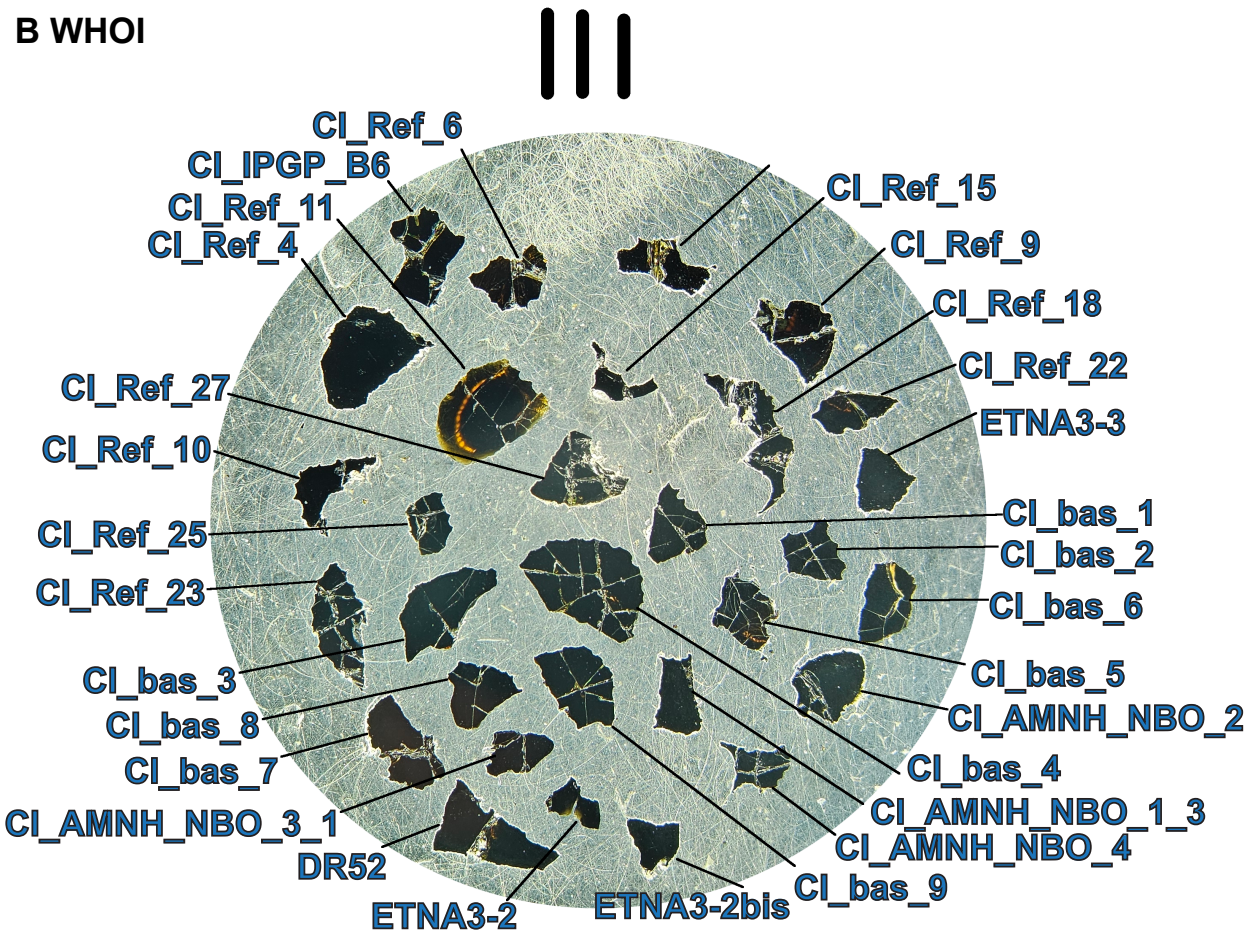

Fig. S2. The map of the sample mounts used for (A) Nancy and (B) WHOI.

Supplementary Table

Table S1
"Best" standards with spatial homogeneity in $\delta^{13}C$ and well within 1σ error for both CO_2 concentration and $\delta^{13}C$– values

Name	Type	[a]External precision < Internal precision + 0.3 ‰	[b]CO_2 concentration	[c]$\delta^{13}C$	External precision < Internal precision + 0.3 ‰	CO_2 concentration	$\delta^{13}C$	[d]Best standards
			Nancy			WHOI		
CI_Ref_4	MORB				*	*	*	*
CI_Ref_6	MORB	*	*	*	*	*	*	*
CI_Ref_9	MORB	*	*	*	*	*	*	*
CI_Ref_10	MORB	*	*	*	*	*		
CI_Ref_11	MORB	*	*	*	*	*	*	*
CI_Ref_15	MORB	*						
CI_Ref_18	MORB		*	*				
CI_Ref_20	MORB	*	*	*				*
CI_Ref_22	MORB	*	*	*				*
CI_Ref_23	MORB	*	*		*	*	*	*
CI_Ref_25	MORB	*	*	*				*
CI_Ref_27	MORB	*	*			*	*	
CI_Ref_28	MORB		*					
CI_bas_1	Basanite	*	*	*	*	*	*	*
CI_bas_2	Basanite	*	*		*	*	*	*
CI_bas_3	Basanite	*	*	*	*	*	*	*
CI_bas_4	Basanite	*		*				
CI_bas_5	Basanite							
CI_bas_6	Basanite	*		*	*		*	
CI_bas_7	Basanite	*		*				
CI_bas_8	Basanite	*		*				
CI_bas_9	Basanite	*		*				
CI_AMNH_NBO_1_3	NBO				*		*	
CI_AMNH_NBO_2	NBO				*		*	
CI_AMNH_NBO_3_1	NBO				*		*	

Continued Table S1

Name	Type	[a]External precision < Internal precision + 0.3 ‰	[b]CO_2 concentration	[c]$\delta^{13}C$	External precision < Internal precision + 0.3 ‰	CO_2 concentration	$\delta^{13}C$	[d]Best standards
		Nancy			WHOI			
CI_AMNH_NBO_4	NBO				*		*	
DR52	Test (DR52)_		*		*	*		
ETNA3−2	Test (ETNA)		*		*	*	*	*
ETNA3−2bis	Test (ETNA)				*	*	*	*
ETNA3−3	Test (ETNA)		*		*		*	
CI_IPGP_B6	Test (Hawaii)		*	*	*	*	*	*

[a] Spatial homogeneity in $\delta^{13}C$ –marked sample show external precision < internal precision + 0.3 ‰.
[b] Well characterized for CO_2 – marked sample are within the 1σ envelop on the CO_2 calibration plot in Fig. 8, showing CO_2 concentration measured by FTIR versus $^{12}C/^{18}O$ measured by SIMS.
[c] Well characterized for $\delta^{13}C$ –marked samples are within the 1σ of the 1:1 line in Fig. 7, comparing $\delta^{13}C$–value measured by SIMS versus EA-IRMS.
[d] The samples are marked if they meet the above three criteria during either sessions in Nancy or in WHOI.